WILEY ONLINE LIBRARY

Early View publication on wileyonlinelibrary.com
(issue and page numbers not yet assigned;
citable using Digital Object Identifier – DOI)

LASER & PHOTONICS REVIEWS

Laser Photonics Rev., 1–25 (2011) / **DOI** 10.1002/lpor.201100002

Abstract In this review, self-mixing interferometry (SMI), a new configuration of interferometry, is discussed. SMI has practical advantages compared to standard interferometry, for example SMI does not require any optical part external to the laser chip and can be employed in a variety of measurements. Applications range from the traditional measurements related to optical path-length – like displacement, small-amplitude vibrations, velocity – to sensing of weak optical echoes – for return loss and isolation factor measurements, CD readout and scroll sensing – and also, a special feature because of the interaction with the medium, measurements of physical parameters, like the laser linewidth, coherence length, and the alfa factor. Because it is also a coherent detection scheme, the SMI works close to the quantum limit of the received field, typically –90 dBm, so that minimum detectable amplitudes of 100 pm/$\sqrt{}$Hz are currently achieved upon operation on diffusive targets, whereas a corner cube allows half-wavelength counting mode – or 0.5 µm resolution – on a dynamic range up to 2 m and more. With its compact setup, the

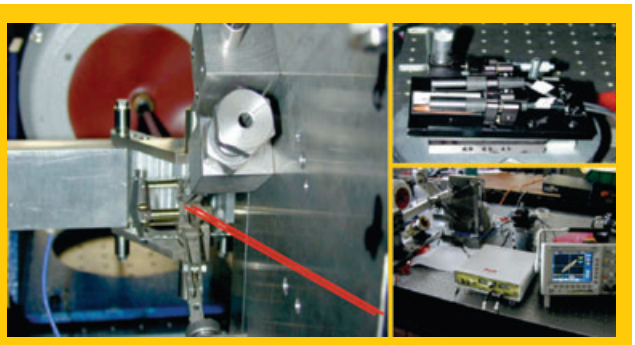

SMI is easy to deploy in the field and can interface a variety of experiments – from MEMS testing to rotating machines vibration testing to pickup of biological motility. The illustration shows a double-channel, differential SMI incorporated in a thermomechanical test equipment to trace the mechanical hysteresis cycle of the beads of a motor-engine brake.

Developing self-mixing interferometry for instrumentation and measurements

Silvano Donati

1. Introduction

Self-mixing interferometry is a new method for the measurement of the optical phaseshift of a remote target. In contrast to methods that employ the laser as the source and an optical interferometer to split and recombine the beam, self-mixing is based on the interaction of cavity field with the field backscatter from the target, what is known as a special case of coupling phenomena.

In general, we get coupling when a small fraction of the field is injected into the laser cavity, either from a physically different laser or from a delayed portion of the laser field itself, as shown in Fig. 1. Coupling phenomena have attracted the interest of researchers since the early days of the laser, because of the theoretical problem of interaction as well as for the potential applications.

The first were the Nobel Prize laureate H. Lamb Jr. and M. B. Spencer, who published in 1972 a pair of seminal papers describing both the three-mirror laser (or self-injection) [1] and the mutual (two sources) injection case [2].

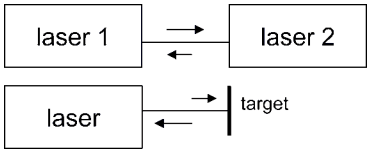

Figure 1 Basic scheme of *mutual coupling* (top), and *self-coupling* (bottom).

The analysis was carried out based on the slowly varying description of field amplitude E and phase φ of the oscillating field, what we call today the Lamb's equations of the laser. Lamb's equations are well suited to gas and crystal lasers in which E and φ are decoupled from the density of states N, whereas in a semiconductor laser we shall add a third equation to describe the carrier concentration and its dependence on E and φ, getting the modified Lamb (or Lang and Kobayashi) equations [3–5]. Despite the difference, interestingly the main results found with the Lamb's equations still hold and correctly describe coupling phenomena for any type of laser, including the semiconductor laser diode.

A classification of systems based on coupling, as shown in Fig. 1, is that of *mutual*-coupled and *self*-coupled systems. Mutual-coupled system are the paradigm of oscillator synchronization and may be *symmetrical* or *asymmetrical* (a master/slave system when an optical isolator is inserted between the sources).

Another classification is according to the *strength* of coupling. We say coupling is *weak* when the perturbing field brought back into the laser cavity is a fraction of, say, down to 10^{-8} and up to 10^{-2}, of the pre-existing field power.

In the weak regime of self-coupling, the main phenomenon is amplitude (AM) and frequency (FM) modulation of the oscillating field, with a driving term (or modulation index) proportional to the fraction of returned field and to the sine or cosine of the optical phaseshift $2ks$ (k

Department of Electronics, Università di Pavia, Pavia, Italy
* Corresponding author: e-mail: silvano.donati@unipv.it

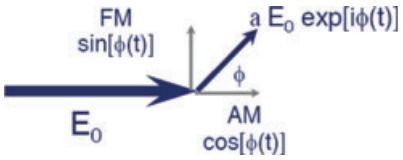

Figure 2 (online color at: www.lpr-journal.org) Self-coupling interaction can be represented by a rotating-vector addition, with a small returned component a $E_0 \exp i\varphi$ dynamically added to the cavity field E_0: the in-phase component $\cos\varphi$ generates AM modulation, whereas the in-quadrature component $\sin\varphi$ is responsible for FM.

= wavevector, s = distance) external to the perturbed laser. This is the case studied by Spencer and Lamb in [2]. In applications, we will readily take advantage of weak coupling in self-coupled systems by making out of it very sensitive echo sensors and interferometers.

Before proceeding, let us explain the self-mixing modulations as the result of rotating-vector addition [5] as in Fig. 2. Let E_0 be the unperturbed cavity field, and $aE_0 expi2ks$ the field back from the target, a being the attenuation and $2ks$ the phase delay of propagation. As is well known from communication theory, rotating vector addition generates an AM modulation driven by the in-phase component of the modulating term, that is $aE_0 \cos 2ks$, and an FM by the in-quadrature component, or $aE_0 \sin 2ks$.

In applications, while the AM is readily available from the intensity (or power) detected by a photodiode, FM is difficult to retrieve because is impressed onto the optical frequency (it requires frequency downconversion, see Sect. 3.2.3).

Also in the weak regime of mutual-coupling we find AM and FM in each of the two interacting lasers, and the driving terms are now the ratio of amplitudes and the frequency difference of the two waves [6]. The coupled system can then be regarded as a special coherent detector receiver, also called an injection detector [4].

Going back to classification, we say coupling is *strong* when the exchange is a fraction up to several per cent of the pre-existing oscillation power. Even at this apparently modest level of injection, the AM and FM modulations become so strong that they drive the laser out of a reproducible regime of oscillation, entering a nonlinear high-level dynamic regime [7], in both the mutual- and self-coupling cases. This regime is highly characteristic of a *complex* system and is heralded by new unexpected behaviors such as bifurcations, multiperiodicity and chaos in mutual-coupled systems, and relaxation oscillations, bistability, multistability, and chaos in self-coupled systems.

No wonder then, the Lang and Kobayashi equations for the laser are similar to the Lorenz and Lorentz equations for turbulence in a fluid, the canonic system generating chaos dynamics.

Fortunately, the high-level dynamics can be still described by small-perturbation analysis, or, the Lang and Kobayashi equations still apply at strong level and fully account for the observed complexity and chaos regimes [7].

In applications, the regimes of strong coupling are of importance to develop new techniques like optical chaos generators, chaos masking, synchronization, and chaos-cryptography systems.

Because a remote mirror can also be regarded as a source of feedback, schemes based on self-coupling have been variously referred to as *feedback*, *induced-modulation*, *injection*, and *self-mixing* interferometers. This is the subject covered in this paper, which is organized as follows. In the next section we introduce the basic ideas underlying a self-mixing interferometer, and summarize the methods to analyze it. In Sect. 3 we develop the applications of self-mixing to a variety of kinematic measurements (displacement, vibrations, velocity), and in Sects. 4 and 5 we describe the measurements of some physical quantities of the laser (linewidth, alfa factor), and last but not least, as a remote echo detector; finally we draw some conclusions.

2. Description of the self-mixing interferometer (SMI)

The basic setup of a self-mixing interferometer is shown in Fig. 3: the beam from a laser diode is shone onto a remote target and a fraction $1/A$ of the emitted power P_0 is collected back into the cavity, where it leads to modulation of the cavity field. A photodiode detects the AM-modulated, interferometric signal contained in the beam power.

The practical implementation of a SMI is similar to its very simple schematic: as a detector we customarily use the monitor photodiode already provided in the laser diode package by the manufacturer, whereas on the front output we just need a collimating optics (the plastic molded lens offered by the manufacturer is adequate) and eventually an attenuator to adjust the level of retuning signal. Often, the target need not be reflective, as the weak backdiffused signal from a plain diffuser surface is usually large enough.

The only care to exercise is that the laser works in a single longitudinal mode regime, and is biased well above threshold so as to have low side-mode content: this ensures a clean SMI waveform.

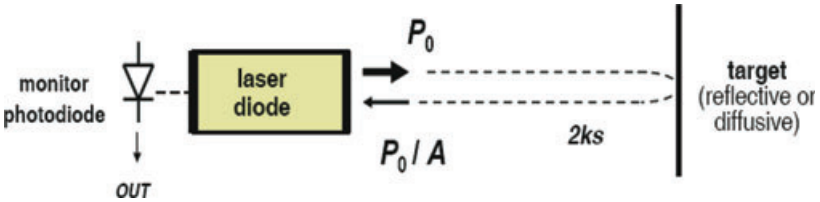

Figure 3 (online color at: www.lpr-journal.org) Schematic of a self-mixing interferometer (SMI) using a laser diode.

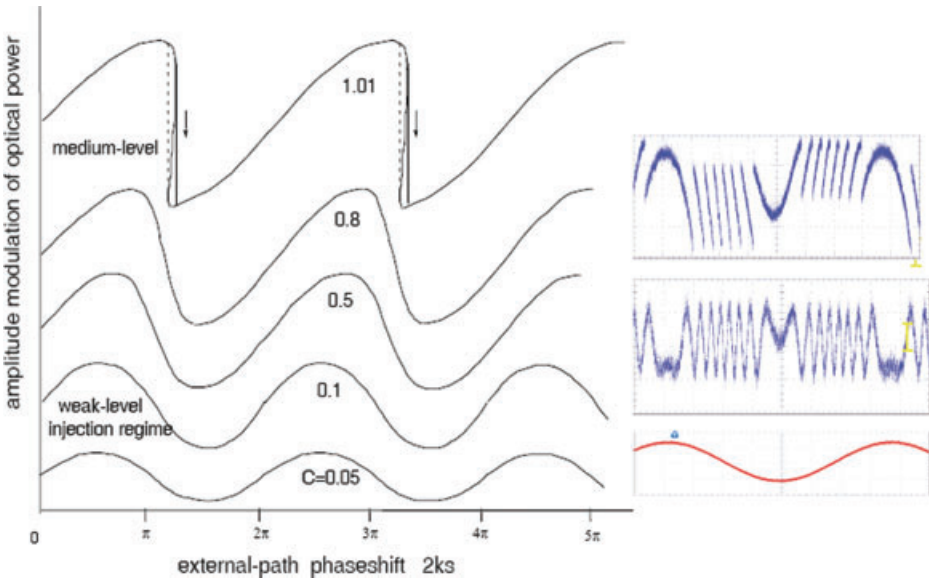

Figure 4 (online color at: www.lpr-journal.org) SMI waveforms for weak to moderate level of coupling. Left: calculated results; right experimental waveforms for a sine-wave driving. Up to $C \approx 0.1$ the waveform is much a cosine function of the optical phaseshift, then at increasing C it becomes progressively distorted until at $C = 1$ a switching appears in the trailing edge, marking the onset of ECM (external cavity mode). Regimes are those used in applications such as: 2-channel interferometer, LDV ($C \ll 1$), fringe-counting SMI ($1 < C < 4.6$), and also alfa-factor, linewidth measurement, and angle measurements.

Now, because of the self-mixing process in the cavity, the resulting emitted power can be written [8] as:

$$P = P_0[1 + m_A F(\varphi)], \tag{1}$$

where P_0 is the unperturbed power, $\varphi = 2ks$ is the optical phase shift suffered on propagating to the target distance s and back, with $k = 2\pi/\lambda$ the wavevector, and m_A is the amplitude modulation index whose expression is found [8,9] as

$$m_A = A^{-1/2}[c/2s(\gamma - 1/\tau)], \tag{2}$$

γ being the gain per unit time of the medium and τ the cavity decay time. Note that the $-1/2$ dependence on power attenuation A is a clear sign that the SMI process depends on *field*, not *power*, and so it is a *coherent* process [10]. (Explicitly, $A^{-1/2} = a$ is the field attenuation used in Fig. 2.)

Finally, in Eq. (1), F is a function depending on the strength of coupling, yet always a 2π-periodic function of its argument $2ks$. So, we have a full period of the power waveform swing for a variation of target distance $2k\Delta s = 2\pi$ or, solving for Δs, $\Delta s = \lambda/2$ – just like in a normal interferometer. Function F is a plain cosine function of φ at very weak coupling strength, whereas at weak or moderate coupling F becomes a distorted cosine wave (Fig. 4).

Following Acket et al [11], we can introduce an *injection parameter* C to describe the strength of coupling as follows:

$$C = (1 + \alpha^2)^{1/2} A^{-1/2} \kappa s / n_{\text{las}} L_{\text{las}}, \tag{3}$$

where

$$\kappa = \varepsilon \delta (1 - R_2)/\sqrt{R_2} \tag{3a}$$

is the fraction of field coupled back and interacting with the laser mode. In Eqs. (3) and (3a), α is the linewidth enhancement factor of the laser, ε is the mode superposition factor, R_2 is the output mirror (power) reflectivity, δ the (field) target diffusivity (if not already included in A), s the target distance, n_{las} and L_{las} the effective index of refraction and the cavity length of the laser, respectively.

About the waveform $F(\varphi)$ of the SMI signal, starting from weak coupling, $C < 0.01$, F is initially a cosine wave as in a normal interferometer, but as C increases the waveform becomes progressively distorted, with the trailing edge steeper than the leading edge (Fig. 4) [5,8], up to the critical condition $C = 1$ when a switching appears in the trailing edge. The regime of SMI with one switching per period is important and corresponds to *moderate coupling*, a preferred condition for SMI operation.

On continuing to increase C, we reach $C = 4.6$, when a second switching shows up in a $2ks$ period. Further increase of coupling brings about additional switchings, see Fig. 5, up to the point that waveform becomes erratic, because one of a multiple choice of switchings to be sorted will depend critically on initial conditions of the system – the system enters a regime of multistability and chaos.

To develop interferometry measurements, we work up to $C < 4.6$ but usually at $C \ll 1$ to have an easily processed signal. There is no reason to work at $C > 4.6$ and face the problem of multiple switchings per period when making measurements, also because peak-to-peak amplitude of the SMI waveform (and the SNR) is no longer improved. We go at high values $C >$ 20–50 when we wish to generate optical chaos.

About the signal pickup, the most convenient to use is the rear output of the laser, as shown in Fig. 3, where the manufacturer usually provides a photodiode (with tilted surface) for output-power monitoring. Yet, if the rear PD is missing, as in VCSELs, we can place a photodiode on the front output beam, and eventually detect the SMI signal at the target location.

When using the front output, we shall avoid falling on a zero of the SMI signal [12,13]. Vanishing of the self-mixing signal is found at a certain bias current, at which the outgoing field is cancelled by an opposite-phase, backreflected field bouncing back at the output mirror, (see details in [12]). Finally, if PDs are not practicable, we can also read the SMI signal as a (small) voltage superposed to the quiescent bias

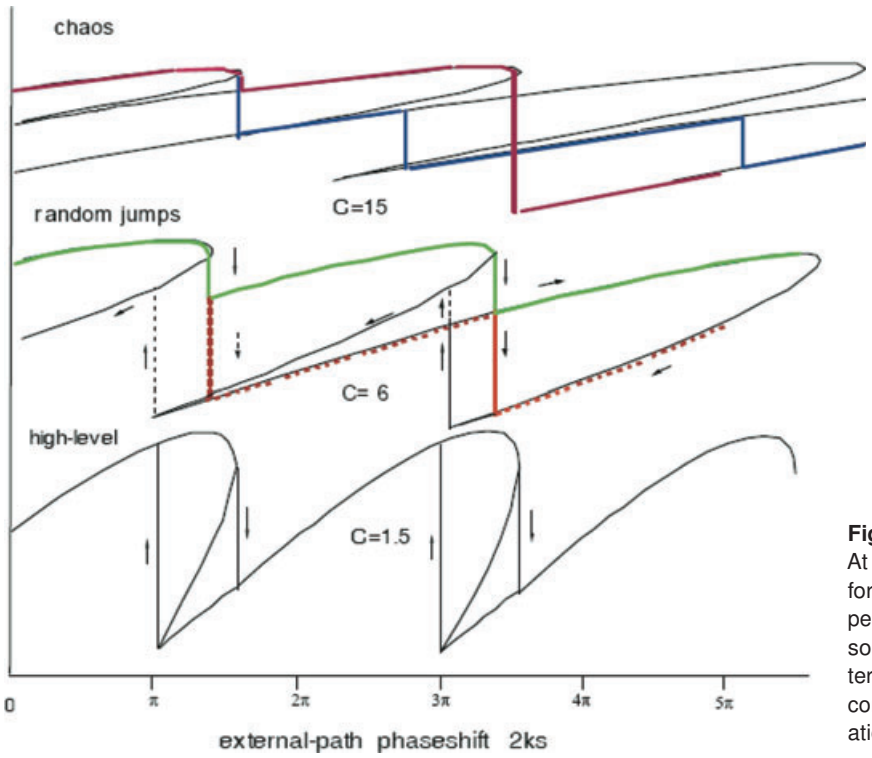

Figure 5 (online color at: www.lpr-journal.org) At even increasing values of C, the SMI waveform first displays more than one switching per period of 2ks, and then multiple switchings soon becoming erratic. The system then enters the chaos regime of oscillations, no more convenient for SMI but useful for chaos generation, synchronization, and cryptography.

voltage [12, 13], though the S/N ratio there is not as good as at the rear and front outputs.

2.1. Analyzing self-mixing phenomena

Basically, three methods are available to analyze self-mixing phenomena. One, the *rotating-vector* addition (Section 1), simply explains the AM and FM sine and cosine dependence of the SMI signal.

Secondly, the *3-mirror* model analyzes the optical feedback in view of the theory of oscillators (Fig. 6), considering the target as a retroreflecting element and applying the steady-state Barkhausen condition of oscillations. To do that, let us write the perturbed loop gain of the laser oscillator as a balance starting at mirror M1:

$$G_{\text{loop}} = r_1 r_2 \exp 2\alpha^* L \exp i2kL + a \exp i2ks\,, \qquad (4a)$$

where r_1 and r_2 are the mirror (field) reflectivities, $\alpha*$ and L are the (field) gain per unit length and the length of the laser, and a is the field attenuation of the external target.

First, letting $a = 0$ in Eq. (4a), we get $G_{\text{loop}} = r_1 r_2 \exp 2\alpha * L \exp i2k_0 L$, for $k_0 = 2\pi n_l \nu_0/c$ and the unperturbed frequency ν_0 of oscillation, n_l being the effective index of refraction of the laser medium.

Now, let's apply the second Barkhausen condition – that the loop gain in the permanent oscillation regime is exactly one – or: $\Re\{G_{\text{loop}}\} = 1$ and $\Im\{G_{\text{loop}}\} = 0$. Using Eq. (4a), and $r_1 r_2 \exp 2\alpha * L \approx \exp -i2k_0 L$, and developing $\Im\{G_{\text{loop}}\} = 0$ we get:

$$\sin 4\pi L n_l (\nu - \nu_0)/c + a \sin 4\pi(\nu/c)s = 0\,, \qquad (4b)$$

or also, being $4\pi L n_l(\nu - \nu_0)/c \ll 1$, and rearranging terms

$$\nu = \nu_0 + (c/4\pi L n_l) a \sin 4\pi(\nu/c)s\,. \qquad (4c)$$

In Fig. 6 (bottom), we plot the diagram of the actual oscillation frequency ν as a function of unperturbed frequency ν_0. Here, as long as the $(c/4\pi L n_l)a$ remains small, or $C < 1$, there is one solution for ν (a stable, single oscillating mode). But, on increasing a, the undulation increases in amplitude and for $1 < C < 4.6$ there are 3 solutions, one unstable (the central one) and two stable [8]. This corresponds to a switching in the waveform, and to the onset of ECM (external cavity modes), starting to be excited at $C = 1$ and increasing in total mode number as $\approx 2C/\pi$.

Equation (4c) can be brought to the form of the standard Adler's frequency equation [6, 8, 14]:

$$\omega\tau = \omega_0\tau - C \sin(\omega\tau + a \tan\alpha)\,, \qquad (4d)$$

where $\tau = 2L/c$ is the external time delay, C is the coupling factor (Eq. (3) and α is the linewidth enhancement (in this equation, α is introduced a posteriori). Interestingly, condition (Eq. (4d)) can also be derived from the Lang-Kobayashi equations (see below).

The 3-mirror model explains several interesting results but lacks some details concerning the physical setting of the phenomenon, i. e. the material (semiconductor) and associated effects for a laser diode.

The third approach is the most complete, based on the Lamb's equation for the slowly varying approximation of amplitude and phase of the electric field, and modified with the additional equation for the state concentration, i. e. the *Lang-and-Kobayashi* (L-K) equations [3], which can be

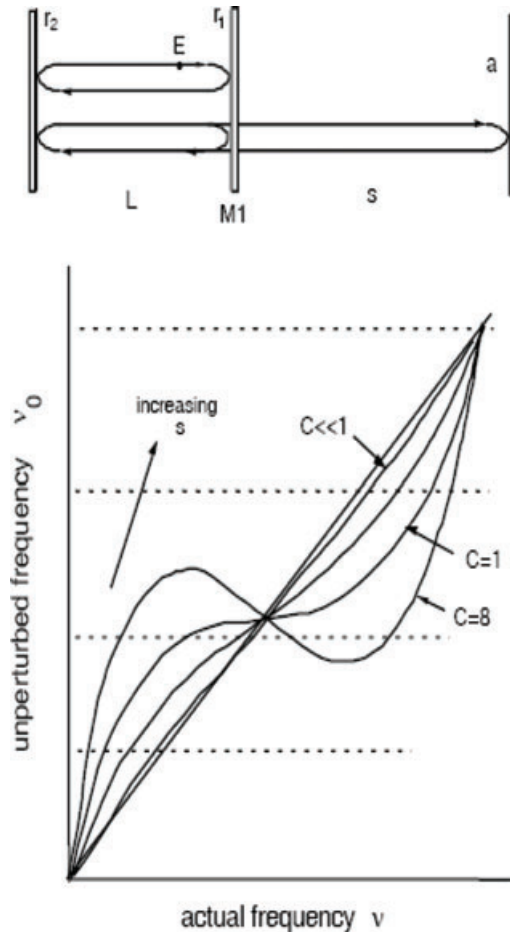

Figure 6 The 3-mirror model (top) and the plot of actual frequency ν to unperturbed frequency ν_0 of the laser: for $C < 1$ there is a single intersection (one stable solution), for $C > 1$ three intersections (two stable and one unstable), and the system starts oscillating on external cavity modes.

written in the following form [5, 8]:

$$\begin{aligned} dE/dt &= \tfrac{1}{2}[G_N(N-N_0) - 1/\tau_p]E \\ &\quad + (\kappa/\tau)E(t-\tau)\cos[\omega_0 t + \varphi(t) - \varphi(t-\tau)]\,, \\ d\varphi/dt &= \tfrac{1}{2}\alpha\{G_N(N-N_{\text{thr}}) - 1/\tau_p\} \\ &\quad + (\kappa/\tau)E(t-\tau)/E(t) \\ &\quad\quad \times \sin[\omega_0 t + \varphi(t) - \varphi(t-\tau)]\,, \\ (d/dt)N &= J\eta/ed - N/\tau_r - G_N(N-N_0)E_i^2(t)\,, \end{aligned} \tag{5}$$

where (with typical values noted):
$\tau = 2s/c$ is the roundtrip propagation delay,
G_N = modal gain $= 8.1 \times 10^{-13}$ m^{3}s^{-1},
κ = fraction of field coupled to the oscillating mode (Eq. (3a)),
N = carrier concentration (m^{-3}),
N_{thr} at threshold $= 2.5 \times 10^{24}$ m^{-3},
N_0 at inversion $= 1.2 \times 10^{24}$ m^{-3},
τ_p = photon lifetime in cavity = 2 ps,
τ_r = carrier lifetime = 5 ns,
α = linewidth enhancement factor = 3 – 6,
ω_0 = unperturbed frequency $= k_0/c$,
$J\eta$ = pumping current density and internal quantum efficiency on the active layer thickness d.

The L-K equations are point-independent equations describing the active material, quite different from the 3-mirror system-based equations. Yet they carry a description of a laser oscillator through the coupled terms (those multiplied by κ) and the delayed terms $E(t-\tau)$ and $\varphi(t-\tau)$.

The L-K equations surprisingly yield all the results already discussed above and found with other approaches, including Adler's equation (Eq. (4d)).

Solutions of the L-K equations reveal: the AM/FM modulations, the $F(\varphi)$ waveforms, the C factor as the break point of switching, (see [5] for detailed calculations), incipient bi- and multistability, line broadening and narrowing, route to chaos [7], etc. When compared to experiments, the L-K equations are found to give a remarkably accurate modeling of both the weak-level SMI phenomena and the high-level chaos-related dynamics. The only deviation is a larger than predicted linewidth of oscillation, reconciled with experiment, as first proposed by Henry, with the introduction of an *a-posteriori* linewidth enhancement factor α [15] in the L-K equations, on the second line of Eq. (5).

As a final remark, we can use the diagram introduced by Tkach and Chraplyvy [16] who first described the feedback effects, later also discussed by Petermann [14] with reference to communication applications. In the diagram (Fig. 7), SMI phenomena are located at the left bottom corner, whereas chaos for cryptography is in the topmost region. SMI obviously requires coherence of the returning field addition to the in-cavity unperturbed field, whereas chaos can be generated also from incoherent coupling (because field E is coupled to concentration N, see the last of Eq. (5)). In Fig. 7 we have drawn the lines at constant C (cf. Eq. (3)) for a typical laser diode. Also shown is the characteristic length $L_{\text{freq}} = c/2f_2$, associated to the high-frequency (modulation) cutoff f_2 of the laser diode, separating the short ($s < L_{\text{freq}}$) cavity regime with continuous frequency spectrum of the chaos, from the long ($s > L_{\text{freq}}$) cavity regime with spike-like spectrum.

2.2. Features of SMI interferometer – advantages and disadvantages

Well-established interferometers [17, 18] used in applications (such as instrumentation, avionics, etc.), fall into one of two configurations, depending on the position of the source respect to the optical interferometer: the *external* (Fig. 8, upper left) or the *internal* (Fig. 8, lower left).

Analyzing these configurations [17], we find that the optical pathlength $2ks$ is read on an amplitude output signal of (for the external) and on a frequency output signal (for the internal), respectively.

In a self-mixing interferometer, interaction with the backreflected weak field generates in AM and FM modulations of the emitted field. The modulation indexes are the

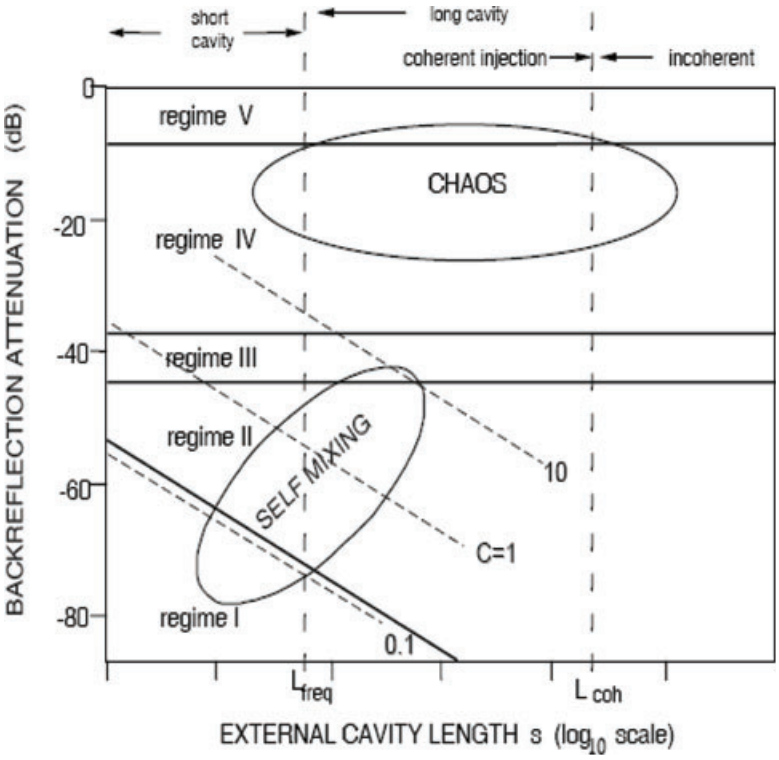

Figure 7 In the diagram of coupling-strength (backreflection attenuation) versus external cavity length, applications of SMI phenomena are located in the lower left side, whereas high level dynamics effects (multi-periodicity and chaos) are mostly in the upper part of the diagram. According to the original description of Tkach and Chraplyvy, regime I corresponds to linewidth narrowing/broadening (depending on the phase of feedback), II to line splitting and mode-hopping, III to return to single-mode narrow-line operation, IV to cohereence collapse, V to external cavity mode. Dotted lines represent constant C for a typical laser diode. L_{freq} is the relaxation length and L_{coh} the coherence length of the laser.

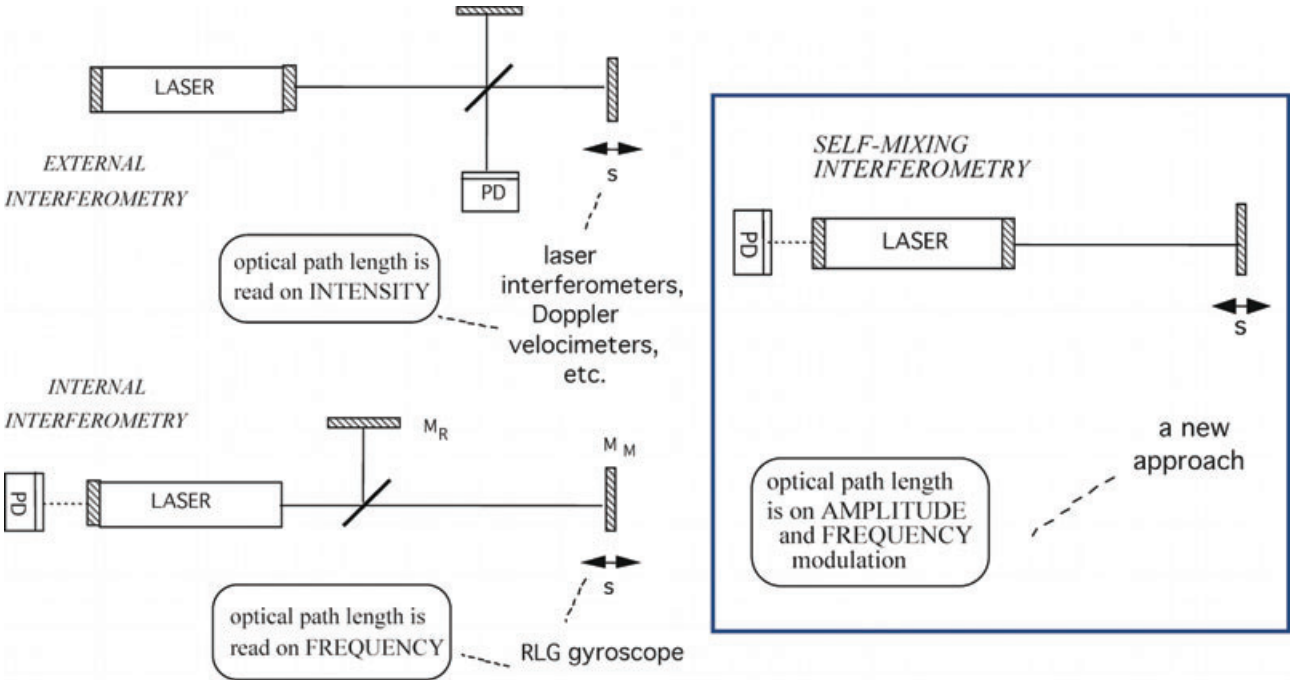

Figure 8 (online color at: www.lpr-journal.org) Compared to conventional schemes of interferometry (left) the *external* used in displacement measurements and velocimeters, and the *internal* used in gyroscopes, self-mixing (right) yields a different output signal, yet containing as AM/FM the same pathlength information, a sine/cosine function of optical phase shift 2ks to the remote target.

$\sin 2ks$ and $\cos 2ks$ signals we exactly need [17] in an interferometer to be able to reconstruct the argument $2ks$ from trigonometric signals without ambiguity. So, in principle, the adequate signals are available to make a new interferometer out of the self-mixing configuration.

From the user's point of view, when compared to the other traditional interferometric configurations, the SMI has inherently these advantageous features:

– optical part-count is minimal (there is no optical interferometer external to the source);

– setup is self-aligned (the SMI makes a measurement where the laser spot falls);
– no spatial, wavelength or stray-light filters required (the Fabry-Perot or DFB cavity of the laser already acts as a filter);
– operates on a normal diffusing target surface (SMI tolerates a relatively strong loss A);
– signal is everywhere on the beam, also at the target side (this is a feature unique to SMI, exploited in special applications);
– resolution is $\lambda/2$ with fringe counting, and sub-λ with analog processing (SMI, like any interferometer, reaches the quantum noise limit of detection, thus minimum detectable displacement is $\ll \lambda$);
– bandwidth is up to hundreds of kHz or MHz (with easy processing).

Of course, there are also disadvantages, like:

– a reference arm is missing (at least in the basic setup);
– wavelength accuracy and long-term stability is poor (with a cheap Fabry-Perot laser diode, the strong λ dependence on bias current and temperature makes it difficult to have $\Delta\lambda/\lambda < 10^{-3}$, thus the measurement has 3 significant digits, not 6–7 as with a HeNe laser [17]);
– little flexibility of reconfiguration (as it is minimum-part count, the SMI can't easily be modified);
– operating on a diffuser target surface, the SMI signal is affected by the speckle pattern statistics (with fading of amplitude, and phase-error effects, see [19]).

2.3. Classification of SMI measurements

Basically, looking at the SMI schematic and waveforms (Fig. 9), we can think a single processing scheme will fit all applications, but this is not the case.

As a first approach, we can make a digital processing of $I_{ph}(t)$, by counting periods of peak-to-peak swing I_{P-P}, which correspond to $\lambda/2$ variations Δs of target distance.

Secondly, we may use an analog processing for $I_{ph}(t)$, because a small observed variation ΔI_{ph} corresponds to a small distance variation Δs, easily seen equal to $\Delta s = (\lambda/4\pi)\Delta I_{ph}/I_{P-P}$.

As the minimum ΔI_{ph} we can appreciate is much smaller than I_{P-P}, (the rms noise σ_{Iph} associated to I_{ph}, see the trace in Fig. 9), resolution is much better with the analog processing, reaching down to nanometers easily, and with 20–50 pm attainable in experiments. (The quantum noise limit is even smaller, in the range of 1–10 fm/$\sqrt{\text{Hz}}$, see [17].)

Yet digital processing is by far superior when we require a large dynamic range. By counting $\lambda/2$ fringes, the dynamic range of measurement is only limited by the number of decades we allocate to the counter. Thus, we can readily attain 5–6 decades of $\lambda/2$ steps, opposite to a I_{P-P} swing corresponding to $\lambda/2$, just one half-wavelength, of the analog.

Therefore, it is customary to classify the SMI as a displacement measuring instrument, when we use digital processing and aim to make a measurement with sub-λ resolution over a large distance – typically up to a few meters – as required for machine tool and mechanical shop applications [18].

On the other hand, if we use the SMI with an analog processing, we will probably be interested in analyzing periodic motions of small amplitude (e. g. up to 1–100 µm peak-to-peak) as required in vibration and mechanical fatigue analysis [17], and then we classify it as a *vibration* measurement, and the instrument as a *vibrometer*.

Note that some authors identify vibrometers as velocimeters, not a good choice given that velocimeters [20] are the well-known laser Doppler or LDV instruments, intended for fluid-velocity analysis and anemometry [20]. (Of course, an SMI can also be designed for a $ds(t)/dt$ measurement of the target, then it will be properly called a velocimeter.)

2.4. Typical applications of SMI

In the last two decades, several applications have been reported of SMI that can be classified as follows:

– metrology: displacement, vibration, velocity, distance, angle;
– measurements of laser parameters: linewidth, alfa factor;
– physical quantities: thickness, refraction index, roughness, mechanical resonance, stress/strain hysteresis;
– sensing: detection of remote echoes, return loss, confocal microscopy sensor, CD/scroll sensors, biological motility.

In the following we review a number of reported applications along with the approaches to solve specific problems of each of them.

As a general comment, SMI techniques offer a very remarkable performance and outperform conventional ap-

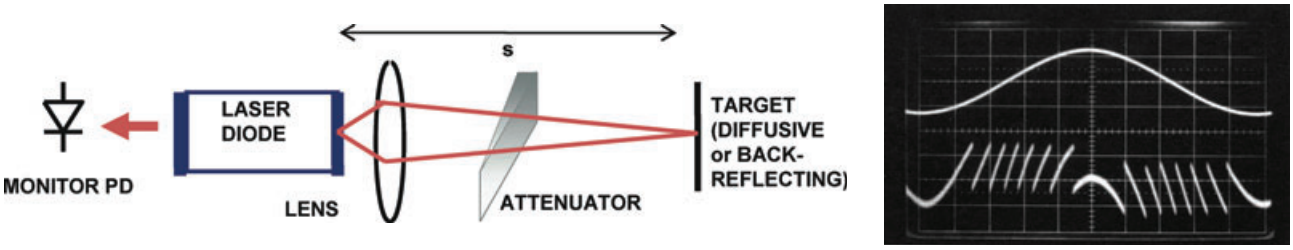

Figure 9 (online color at: www.lpr-journal.org) When the SMI (left) works at $C > 1$, the output signal detected by the photodiode waveform has switching every $\lambda/2$ displacement of the target. The switching is negative-going (bottom trace) when the target is receding (top trace) and is positive-going when the target is approaching. (from [8], courtesy of the IEEE)

proaches, yet with limited flexibility in their range of applicability, because even minor changes of specifications usually require major changes and often a complete redesign of the instrument.

3. SMI application to metrology

3.1. Displacement measurements

In the application called by mechanical workshop metrology, the well-known and undisputed instrument is the so-called "laser interferometer" [17], built around a frequency-stabilized HeNe laser. When used with a corner-cube retroreflector as the target, the instrument offers a 0.1-μm resolution on a several meters displacement, corresponding to a dynamic range $> 10^7$ [18].

The SMI approach to displacement measurement is attractive because it can also work on a diffuser, untreated target surface, replacing the corner-cube, and be much cheaper and simpler to operate. In contrast to a normal laser interferometer that requires two signals, $\cos 2ks(t)$ and $\sin 2ks(t)$ to function properly [17] and be able to recover $s(t)$ from the phase of a sine/cosine function without ambiguity, the SMI has the big advantage of readily providing the sign of the displacement increments when operated in the $C > 1$ regime.

Indeed, as we look at the waveform of the SMI signal of the basic SMI configuration (Fig. 9), we see that the waveform switches every $\lambda/2$ variation Δs of the external distance $s(t)$. Also, the switching is positive(negative)-going when the target approaches(recedes) the source, and this marks the sign of the displacement Δs (positive or negative) to be counted [8, 21].

Thus, the development of a displacement-measuring SMI is straightforward (see Fig. 10): from the photodiode output we go to a transimpedence op-amp amplifier converting I_{ph} in a voltage, then we time-differentiate the signal so as to extract switchings as pulses, and rectify the (+/–) pulses, sending them to separate outputs. On counting the pulses in a decimal up/down counter [8], the counter content is the accumulated displacement $s(t)$ to the target, in units of $\lambda/2$, from the $t = 0$ when the counter is reset, to the current time. To end with a decimal, metric readout, a multiplier of the counter content by $\lambda/2$ is provided.

Using a typical GaAlAs laser diode at $\lambda = 850$, as $\lambda/2 = 425$ nm, we get a resolution of about half a micrometer, more than adequate for most machine-tool positioning and measurements [18]. Also, by keeping the time constant of the differentiator stage short enough (say $\tau = 300$ ns) we can accommodate as many as $\approx 1/\tau$ pulses per second (say 3×10^6) or, be able counting the pulses up to a maximum speed $v = \lambda/2\tau \approx 1.2$ m/s of the target. Finally, the SMI signal is found to be large enough to be detected and processed up to a distance $s \approx 2$ m, even using a diffuser noncooperative surface as a target [8, 21].

Concerning accuracy and precision of the measurement, wavelength stability is the first issue. Careful control of bias current and of temperature allows us to work with a stability down to the ppm (10^{-6}) level in the laboratory environment. Another issue is the speckle pattern statistics, adversely affecting the amplitude of the SMI signal and also introducing phase errors [19].

To evaluate the intrinsic performance of the SMI, we have carried out a set of repeated measurements on a $s = 65$-cm displacement. To avoid speckle errors, measurements were done on a corner-cube target. First, as reported in Fig. 11, we observe an important roll-off with temperature, with a relative rms error $\delta s/s$ of about -95 ppm/°C (1 ppm $= 10^{-6}$). After stabilizing the laser chip temperature with a thermoelectric cooler, data go around the zero line

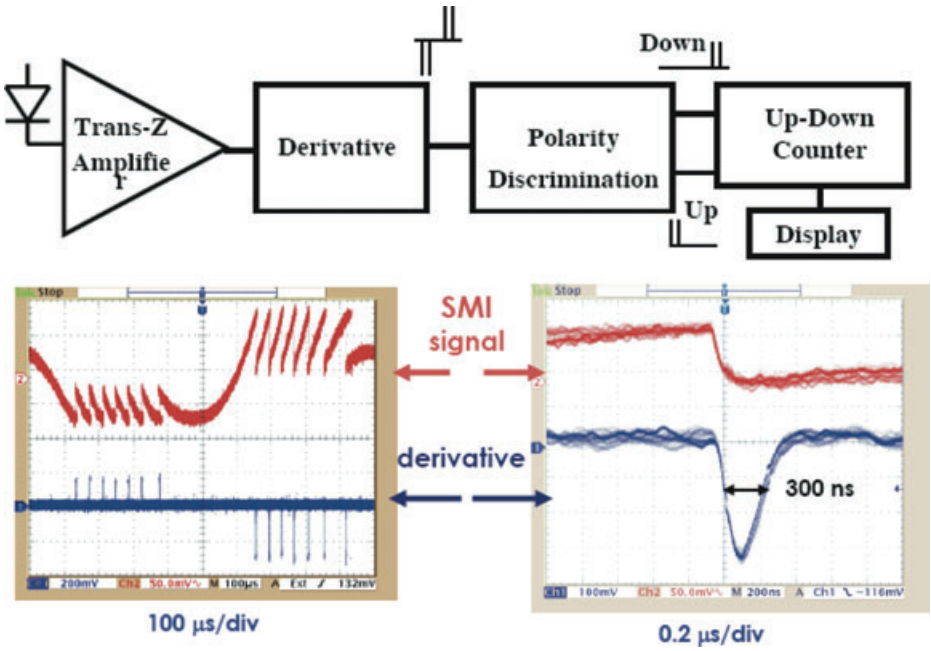

Figure 10 (online color at: www.lpr-journal.org) Schematic of an SMI for measuring displacement with $\lambda/2$-resolution: the photodiode signal is passed through a transimpedance op-amp, time-differentiated and pulses rectified and sorted to the Up /Down input of a decimal counter. A multiplier (not shown) is used to bring the accumulated counting to metric decimal on the display. Typical resolution is 0.5 μm, and maximum speed of the target, with a pulse width of 300-ns, is about 1.2 m/s.

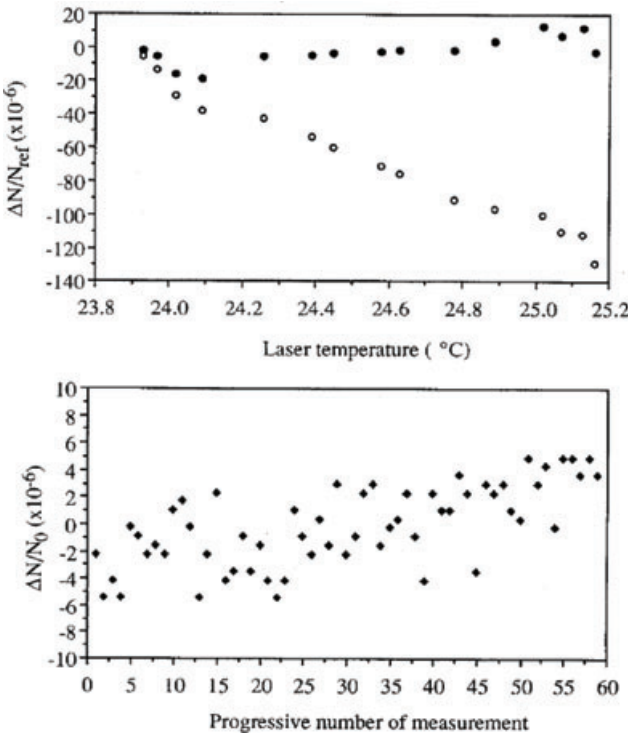

Figure 11 Results of measuring a s=65-cm displacement exhibit a roll-off as a function of diode laser temperature (top, open circles). When temperature is stabilized by a thermoelectric cooler, data returns around zero (top, full dots). The spread over a $N = 60$ sample of measurements lasting 4 hours is about ± 2 ppm (bottom) (from [21], courtesy of the IEEE)

with a spread of about 2 ppm on a set of 60 samples in a 4-h period [21].

Actually, in the practical implementation of the displacement SMI, Fabry-Perot lasers fall short of the ppm-level resolution, because they exhibit wavelength mode hopping (up to $\Delta\lambda = 1$ nm each) at warm-up after switch-on, with a concurrent hysteresis in λ [5]. Instead, DFB laser should be employed, as these sources have been found to be capable of ensuring a ppm long-term (> 1 year) accuracy [21, 22], at least in the laboratory.

With the right laser diode, the SMI performance is thus comparable to that of a traditional HeNe-based instrument [5, 18].

Now we want to go further, and replace the corner cube with a plain diffuser, as permitted by the SMI configuration (whereas this is unwieldy in a normal HeNe-based interferometer, see [5]).

The problem now is that speckle pattern statistics affects the amplitude and phase of the field returning into the laser cavity [23], just the field giving rise to the SMI effect.

An analysis of the phenomenon (see for example [19]) shows that while the phase error can be kept relatively small (e. g., a few λ's on a $s = 1$ m swing), amplitude fluctuations are a serious problem and should be strongly reduced, because they cause the loss of the signal (or, a decrease below the desired $C > 1$ level) and of the associated $\lambda/2$ countings. This happens when we fall on a relatively "dark" speckle during the displacement of the target along the path $s(t)$ under measurement.

More precisely, the probability of getting a speckle amplitude less than k (e. g., 0.01) times the average is just k [19, 23]. So, even introducing an AGC (automatic gain control) on a range G, there is always a small probability of fading, i. e. of the signal becoming so small as to be lost (e. g., a probability of $0.01/G$).

One idea for mitigating speckle fading is to take advantage of the statistics itself: alongside a dark speckle there are probably other more intense, brighter speckles. If we arrange a minute deflection of the spot projected onto the target, large enough to change the speckle sample but small enough that the distance under measurement is unchanged, we may be able to move away from the "dark" speckle fading.

The deflection can be performed by a pair of small PZT piezoactuators holding the objective lens and moving it along the X-Y axes, and a servocircuit that, after the detection, closes the loop and feeds the piezo so as to keep the SMI signal maximized [24].

The technique is called BST (bright speckle tracking) and an example of the results is shown in Fig. 12, where, under a normal working condition, a "dark" speckle is found between $s = 74$ and 78 cm, with the amplitude becoming so small that counts are lost. With the BST circuit on, the dip at 76 cm is avoided and counts are registered correctly. (We can also see in Fig. 12 a step up at about $s = 73.5$ cm where the system decides to jump to a brighter adjacent speckle.)

To be rigorous, also with BST we get a reduction but not elimination of the fading probability. Yet, as we may go down to a value $\approx 10^{-6}$ from $k = 0.01$, (see [24] for details), we make the SMI-BST instrument operation on a plain noncooperative diffuser acceptable from the practical point of view, with meter-swing capability and $\lambda/2$ resolution, as implemented in a prototype instrument (see [25]).

3.2. Vibration measurements

When the displacement to be measured is a periodical motion of small amplitude and a frequency range – say from audio to MHz, counting $\lambda/2$ steps is too rough and we may prefer an analog processing of signal $s(t)$.

To start with, the analog format has a dynamic range limitation – a typical op-amp circuit can accommodate signals ranging from mVs (the offset limit) to tens of volts, or have a 10^4 dynamic range – thus, two or three decades less than digital processing in a displacement interferometer with 6–7 decades.

Yet, we can significantly improve the sensitivity to small displacements, well beyond the $\lambda/2$ limit and go down to noise limits of the detected signal.

From this point of view, the minimum detectable displacement or NED (noise equivalent displacement) is easily found [17] noting that the detected signal

$$I_{ph} = I_{ph0}(1 + \cos\varphi)\,, \tag{6}$$

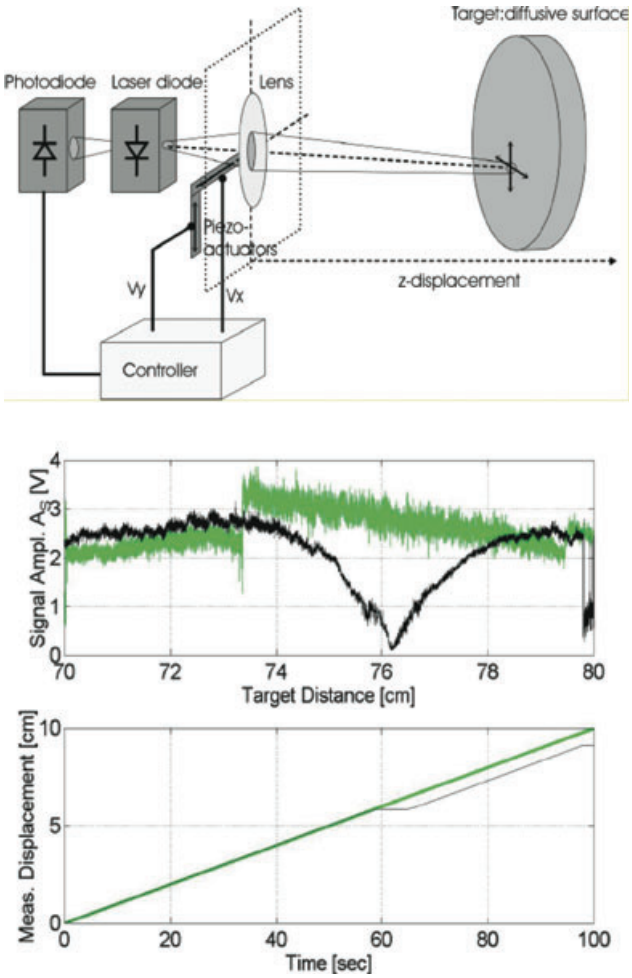

Figure 12 (online color at: www.lpr-journal.org) In the technique called BST – Bright Speckle Tracking – the objective lens is slightly moved it along the X and Y axes by a pair of PZT actuators so as to track the local maximum of intensity scattered by the diffuser back into the laser (top). In an experiment demonstrating BST control, a dark speckle affecting a counting loss at $s = 76$-cm is avoided and the corresponding error is removed (bottom). (from [24], courtesy of the IEEE)

where $\varphi = 2ks$, has maximum sensitivity to phase at the half-fringe point ($\varphi = \pi/2$) where $(\Delta I_{ph}/I_{ph0})^2 = (\Delta\varphi)^2$. Recalling the expression for the shot noise associated with the detected current, that is $(\Delta I_{ph})^2 = 2eI_{ph0}B$ [4], we readily get for $\Delta\varphi$:

$$\left\langle (\Delta\varphi)^2 \right\rangle = 2eB/I_{ph0} = \mathrm{SNR}^{-1}\,, \tag{7}$$

where SNR is the signal-to-noise ratio of the amplitude (i. e. photocurrent) measurement. Using $\Delta\varphi = 2k\Delta s$ and $k = 2\pi/\lambda$ gives [17]:

$$\mathrm{NED} = \left\langle \Delta s^2 \right\rangle^{1/2} = \lambda/2\pi[eBI_{ph0}]^{1/2} = \lambda/4\pi\,\mathrm{SNR}^{1/2}\,. \tag{8}$$

Putting numbers into Eq. (8) reveals [17] that the minimum detectable displacement can go down to nanometers for detected currents of μAs and bandwidth of MHz, and even to picometers for mAs and kHz. These limits are reached or approached substantially in practice, provided we first cure a number of much larger sources of disturbance and interference commonly found in processing circuits.

There are also other fundamental limits to the minimum signal that can be measured by an interferometer, notably coherence, speckle statistics and thermodynamic fluctuations, yet they can be managed to be negligible in a well-designed SMI, and we refer the interested reader to [17] for more details.

Now, there are basically two approaches to implement a small-signal *vibrometer* by analog-signal processing, that is:

(i) Readout at *half-fringe*, so as to take advantage of the *linear conversion* offered by the phase-to-current relationship of Eq. (6) when the interferometer is read in quadrature. To this end, we shall set the quiescent working point of the interferometer in the middle of the cosine amplitude swing, around $\varphi = \pi/2$. Indeed, letting $\varphi = \pi/2 + 2ks$ in Eq. (6), the signal is

$$I_{ph} = I_{ph0}(1 + \cos\varphi) = I_{ph0}(1 - \sin\varphi) \approx -I_{ph0}\varphi$$

for small φ. Then, for small displacements it is

$$\Delta I_{ph} = -I_{ph0}\Delta\varphi = -I_{ph0}2k\Delta s\,,$$

i. e. we get a linear relation between Δs and the SMI output signal ΔI_{ph}, and we can read $\Delta s = \Delta\varphi/2k$ directly from the current variations ΔI_{ph} of the detected current. Note that the linear range of response is limited to $\pm\lambda/2$ by the cosine-like function, at least in the basic arrangement.

This technique, known since the early times of conventional interferometry [17], is easy to implement when a reference arm is available, because the half-fringe condition is in this case written as $\cos(\varphi_{\mathrm{meas}} - \varphi_{\mathrm{ref}}) \approx 0$. To achieve this, we adjust the reference path-length to be $\varphi_{\mathrm{ref}} = \Delta\varphi_{\mathrm{mea}}\pi/2$, so that $\cos(\varphi_{\mathrm{meas}}\varphi_{\mathrm{ref}} = -\sin\Delta\varphi_{\mathrm{meas}} \approx -\Delta\varphi_{\mathrm{meas}}$ for small $\Delta\varphi_{\mathrm{meas}}$.

(ii) *Waveform reconstruction* technique. We can solve for $s(t)$ from the measured photocurrent $I_{ph}(t)$, by inverting the general relationship $I_{ph} = I_{ph0}[1 + F(2ks)]$ for $0 < 2ks < 2\pi$ and then using an unfolding algorithm for extending the reconstruction for $N2\pi < 2ks < (N + 1)2\pi$ [26, 27].

In principle, this method can reconstruct $s(t)$ on a relatively large number N of periods, only limited by the accuracy with which the parameters C and α of the SMI (Eqs. (4d) and (5)) are known.

In practice, results reported in the literature are limited to $N \approx 30$–100, or max amplitudes of $s = 50$–$150\,\mu\mathrm{m}$ (peak-to-peak), whereas for small s the residual computational errors are or the order of 5–10 nm [26], much larger than the noise limit attainable in case (i).

3.2.1. Vibration SMI, small amplitude, linear conversion

In an SMI, we don't have available a reference channel to adjust the fringe signal in quadrature, yet we can take advantage of the wavelength dependence of the semiconductor

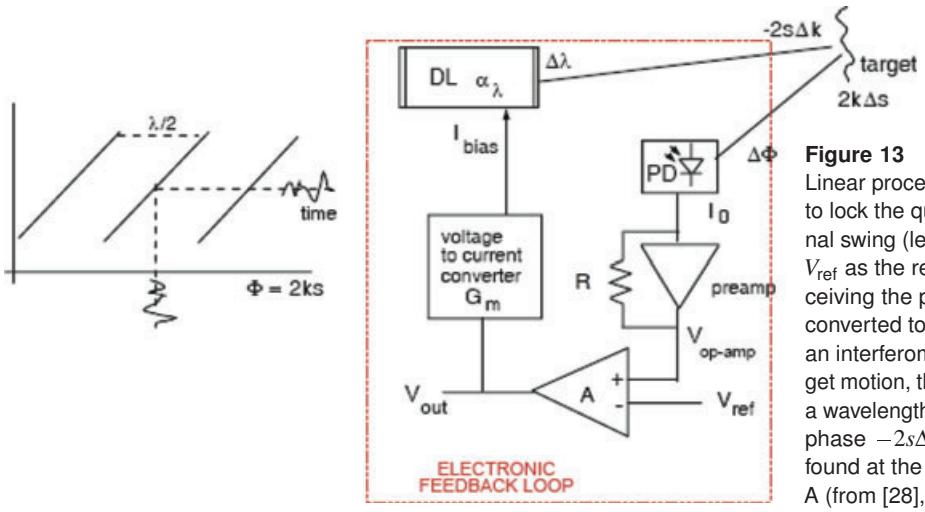

Figure 13 (online color at: www.lpr-journal.org) Linear processing in a small-amplitude vibrometer: to lock the quiescent point at the middle of the signal swing (left) we use the half-fringe voltage level V_{ref} as the reference of the difference amplifier receiving the preamp signal $V_{\text{op-amp}}$. Output is then converted to current and feeds the laser diode. To an interferometric phase variation $2k\Delta s$ due to target motion, the electronic feedback loop reacts with a wavelength change giving an equal and opposite phase $-2s\Delta k$. The vibration signal $2k\Delta s$ is then found at the output V_{out} of the difference amplifier A (from [28], courtesy of the Institute of Physics).

laser from the bias current to develop a control loop and set the working point at half-fringe [28] of the interferometer.

In the moderate feedback regime ($C > 1$) we can use the slow semiperiod of the fringe that is fairly linear (see Fig. 13, left) as the region of operation.

To dynamically regulate the working point at half-fringe, consider the detected signal at the output of the transimpedance amplifier of the photodiode and its amplitude swing, and let V_{ref} be the half-fringe voltage. We use V_{ref} as the reference input of a difference op-amp (block of gain A in Fig. 13) receiving the detected signal $V_{\text{op-amp}}$ at the other input. Then, we amplify the difference and convert it to a current (block G_m in Fig. 13) and send the current to feed the laser diode.

As current I_{bias} impresses a wavelength variation $\Delta\lambda = \alpha_\lambda \Delta I_{\text{bias}}$, and hence a wave number variation $\Delta k = -k\Delta\lambda/\lambda$, we have closed the feedback loop and servoed the phase $2ks$ signal. Indeed, as the target moves, generating an interferometric phase $2k\Delta s$, the feedback loop reacts with a wavelength change yielding an equal and opposite phase $-2s\Delta k$ (if the loop gain is large).

By virtue of the feedback loop, the vibration signal $2k\Delta s$ appears at the output V_{out} of the difference amplifier (Fig. 13, right). This rather surprising result is a consequence of a large loop gain, by which a small difference between V_{ref} and the op-amp output $V_{\text{op-amp}}$ will be exactly the one needed to generate V_{out} and from it the $\alpha_\lambda G_m V_{\text{out}}$ bias current that fulfils the phase-nulling condition $2\Delta ks - 2k\Delta s = 0$.

Thus, we get the vibration signal from the op-amp output ΔV_{out} as:

$$\Delta V_{\text{out}} = [\alpha_\lambda G_m]^{-1}(\lambda/s)\Delta s. \tag{9}$$

Note that, interestingly, the result is independent of the amplitude of the photodetected signal I_{ph} and all its fluctuations, including the target retrodiffuser factor and speckle pattern fading. The only condition is that the loop gain G_{loop} is large. From Fig. 13, the loop gain is easily evaluated as

$$G_{\text{loop}} = RA\alpha_\lambda G_m(s/\lambda^2)\sigma P_0, \tag{10}$$

where $\sigma P_0 = I_{ph0}$ is the mean photodetected current, and σ is the spectral sensitivity of the photodiode.

In practice, in a typical layout of vibrometer [28] we can make $G_{\text{loop}} \approx 500$–$1000$, a condition close to ideality of large gain. More precisely, as a well-known consequence from feedback theory, we can say that residual nonidealities found in the closed loop are reduced by a factor G_{loop} with respect to the nonfeedback condition.

In particular, speckle-pattern fading is nicely reduced by a factor 500–1000, and no longer affects the measurement. (Speckle fading will actually reduce the available loop gain, however, as given by term P_0 in Eq. (10).)

Another beneficial effect of the feedback loop is that linearity and dynamic range are improved by a factor G_{loop} [28]. As is well known from control theory, the dynamic range limit is just an error introduced in the loop, and as such is reduced by G_{loop}. Thus, our small-signal vibrometer does not saturate as the vibration amplitude is larger than a half-fringe (or, $< \lambda/2$). Indeed, as the signal increases and tends to slip out of the fringe, the feedback loop will pull it back, leaving only a $1/G_{\text{loop}}$ residual. So, the dynamic range now becomes $G_{\text{loop}}\lambda/2$, something in the range of 200–500 µm.

An example of performances obtained with a breadboard vibrometer developed from the concept of half-fringe servo loop is reported in [29]. The prototype has a minimum detectable signal of NED = 100 pm (on a $B = 1$-Hz bandwidth) and a max (dynamic range) of ≈ 500 µm. The Wegel diagram of bandwidth/amplitude performance is reported in Fig. 14 along with an example of pickup of vibrations in the field.

Another remarkable application of the half-fringe stabilized, small-amplitude vibrometer worth noting is that to the differential vibrometer, see Sect. 5, for detecting mechanical hysteresis cycle.

3.2.2. Vibration SMI, large-amplitude, waveform reconstruction

We can go to a theoretically unlimited dynamic range of measurement for the signal $s(t)$ if we are able to invert

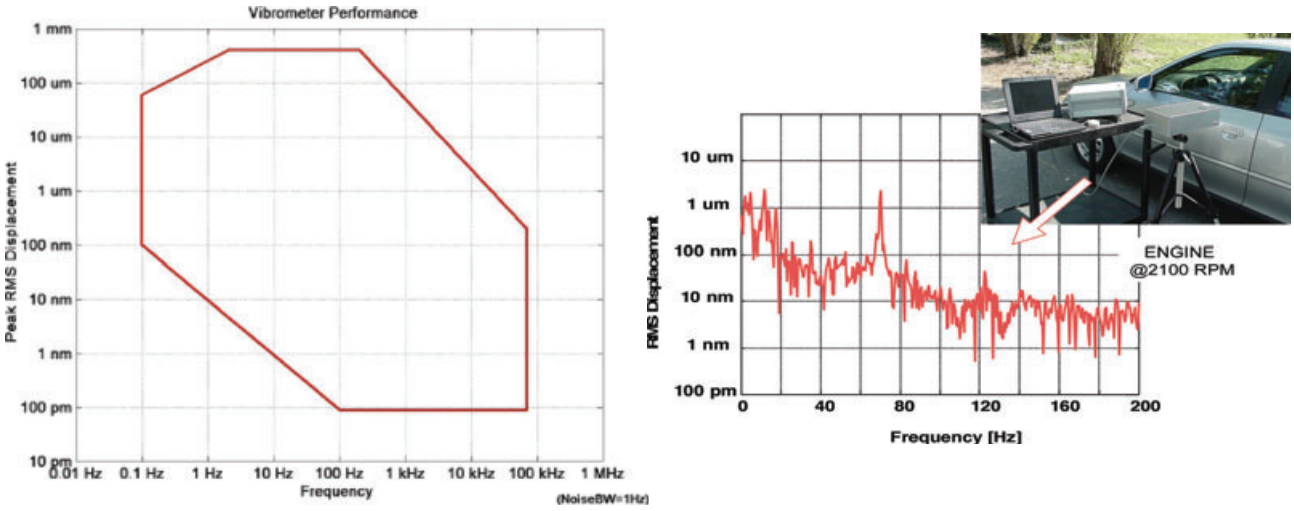

Figure 14 (online color at: www.lpr-journal.org) Left: performance of a half-fringe locked vibrometer: minimum displacement signal is 100 pm ($B = 1$ Hz) and maximum amplitude 500 µm, frequency from 0.1 Hz to 80 kHz (from [28], courtesy of the Institute of Physics). Right: the instrument at work detecting small vibrations on the locked door, as produced by the engine of the car.

Eq. (1) and solve for phase $\varphi = 2ks(t)$ from the measured waveform $I_{ph}(t)$ or $P(t)$.

The algorithm to carry out the inversion has two parts: that relative to the range $-\pi < \varphi < +\pi$, where we shall remove the *nonlinearity* of the F function (Eq. (1)), and that relative to the *unwrapping* of phase when φ goes beyond 2π to the interval $(2N-1)\pi < \varphi < (2N+1)\pi$.

As already noted, when feedback is weak ($C < 1$) and the waveform is practically time-symmetrical, to invert Eq. (1) unambiguously we need two signals, the sine and cosine of $\varphi = 2ks$ (see also Sect. 3.2.3). For this problem, an ample literature is available (see e. g. [30]) about the application of the arccosine function to measured data $I_{ph}(t)$ and its segmentation for phase unwrapping.

When the regime of feedback is moderate and $C > 1$, a single signal is sufficient to carry out the reconstruction, because switchings in the waveform carry the sign of π increments required to unwrap phase. As first proposed in [26], an algorithm can be derived from Eqs. (1) and (4d), that can be applied to the waveform coming from the experimental measurement $F(t) = \Delta P/P_0$ (or $\Delta I_{ph}/I_{ph0}$), and we can retrieve $s(t)$ as:

$$2ks(t) = \pm \arccos F(t) - C\{-\alpha F(t) \pm \sqrt{[1-F(t)^2]}\}/\sqrt{(1+\alpha^2)} + 2m\pi . \quad (11)$$

Here, the sign shall be taken '+' for $dF(t)/dt \cdot (ds/dt) < 0$, and '−' for $dF(t)/dt \cdot (ds/dt) > 0$, and m shall be increased by 1 every two zero crossings of $F(t)$ (for more details see [26]).

Application of Eq. (11) requires the knowledge of parameters C and α. As pointed out in [8], if the linewidth enhancement factor is not too small and the approximation $\alpha^2 \gg 1$ is acceptable, then C can be easily determined from the shape of the $F(t)$ waveform, by looking at the semiperiods of increasing (t_{rise}) and decreasing (t_{fall}) F, whose ratio is found [8] as:

$$t_{\text{rise}}/t_{\text{fall}} = \{\sqrt{(1+\alpha^2)}\pi - 2C\alpha\}/\{\sqrt{(1+\alpha^2)}\pi + 2C\alpha\} \cong (\pi - 2C)/(\pi + 2C) . \quad (12)$$

Additionally, factor α can be either estimated from the type of laser diode, or measured as indicated later in this paper (see Sect. 4.2).

For a typical Fabry-Perot MQW laser diode, with α ranging from 4 to 6, and estimated $\alpha = 5$ for the calculation, application of Eqs. (11) and (12) to a nonsinusoidal periodic waveform $s(t)$ gives the result of reconstruction illustrated in Fig. 15: a 2-µm waveform is reconstructed with a < 5-nm error [26].

A similar result is found when the signal has a much larger amplitude, say N times the wavelength λ: the error remains at < 5–10 nm for N up to 10–20, then for $N < 100$ small inaccuracies in the C factor and in the estimated α factor may entail a π-phase (or $\lambda/2$ amplitude) error in the reconstruction.

A more sophisticated algorithm has been proposed by Plantier et al [27], based on the minimization of a cost function describing the quadratic distance of measured data from a reference waveform calculated theoretically, with adjustable C and α parameters.

Minimizing the error gives the best estimate of C and α, and a self-consistency evaluation confirms the level of accuracy also found with direct analysis of the waveform details reported in Sect. 4.

As a final comment, none of the above algorithms has yet been demonstrated for real-time reconstruction of large-amplitude displacements, say up to the mm or cm ranges, whereas the half-fringe technique (Section 3.2.1) covers well up to the mm or sub-mm amplitudes.

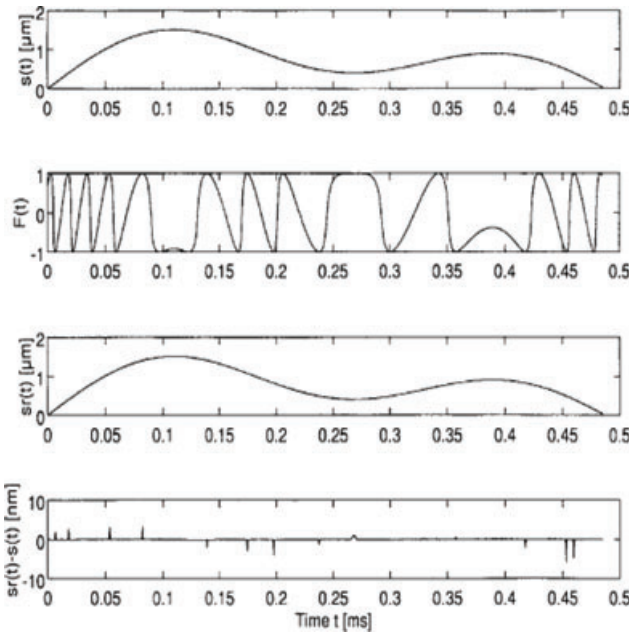

Figure 15 Reconstruction of the s(t) waveform from the measured $F(t) = \Delta I_{ph}(t)/I_{ph0}$: from top to bottom: applied $s(t)$, SMI waveform $I_{ph}(t)$, reconstructed $s_{\text{rec}}(t)$, error $s(t) - s_{\text{rec}}(t)$. For a 2-µm peak-to-peak signal, error keeps $<\pm 2$ nm (from [26], courtesy of the IEEE).

3.2.3. Vibration SMI, large-amplitude, sin/cos reconstruction

A very effective method of unwrapping and reconstruction for either displacement or vibration signals of large amplitude, already known and applicable to all interferometers, is that based on the processing of two orthogonal signals, $\cos 2ks$ and $\sin 2ks$. These two signals are those we look for in a 2-channel laser interferometer [9, 17] to start a digital or analog processing, and are those potentially available in a SMI for $C \ll 1$.

Unluckily, in a laser diode SMI, we are unable to access the $\sin 2ks$ signal, because this is the modulation drive of FM on the optical frequency, out of reach of the direct handling of electrical signal.

On the contrary, if we had a two-mode operation for the laser source, we could use one mode for SMI and keep the other unaltered in the cavity to serve as the local oscillator of a demodulation operation, bringing down to electrical frequency the FM modulation, and making $\sin 2ks$ available for reconstruction.

This is exactly what was done in an early demonstration of self-mixing interferometer dating back to 1977, see [9], the first paper to report an SMI for displacement reconstruction.

To this purpose, we used a HeNe Zeeman laser [17], with the active medium split into two populations, supporting two modes with linear orthogonal polarizations and a frequency difference of 20–100 kHz [9, 17]. Only one mode is allowed to reach the target (see Fig. 16, left) whereas the other is used to downconvert the SMI signal from optical to electrical frequencies, by beating on the rear photodetector. The signal at the photodetector output (Fig. 16, left traces, right panel) shows AM as a small ripple on the amplitude, and FM as a jitter of the sinusoid. After AM and FM demodulations, we get the two signals $S = \sin 2ks$ and $C = \cos 2ks$, see Fig. 16, right traces, right panel [9, 17].

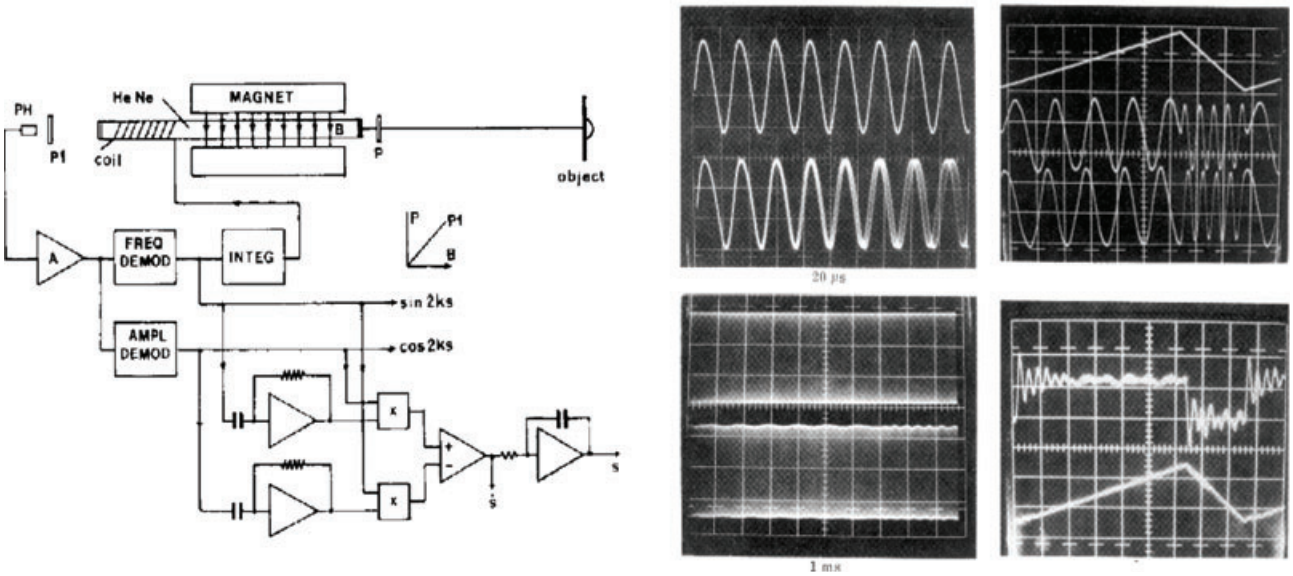

Figure 16 Reconstruction of displacement with the cos/sin signals: (left) we use a HeNe laser with transverse Zeeman effect, creating a pair of orthogonal, linear- polarized modes. A polarizer at the target output selects one mode for self-mixing effect, while the other is kept unaffected in the cavity. A 45-deg oriented polarizer at rear mirror allows beating of the two modes (one carrying the SMI signal, the other a fixed reference) on the photodetector. Amplitude and frequency demodulation reveals the $\cos 2ks$ and $\sin 2ks$ signals (right). We then make the cross product of signals and their derivatives to free out v and then integrate v to obtain s (from [9]).

Reconstruction now proceeds as follows: we make the time derivative of S and C, that is $S' = 2k\mathrm{v}\cos 2ks$ and $C' = -2k\mathrm{v}\sin 2ks$, $\mathrm{v} = ds/dt$ being the time derivative of s. Then, we cross-multiply the derivatives to S and C and subtract the results, thus obtaining

$$S'C - SC' = 2k\mathrm{v}\cos^2 2ks + 2k\mathrm{v}\sin^2 2ks = 2k\mathrm{v}\,,$$

and then we integrate v to obtain s. This algorithm was also reported by Giallorenzi et al. [31].

In Fig. 16, signals v and s are displayed on the bottom right-corner trace. Note that reconstructed waveforms of v, s exhibit a minor ripple with respect to the electrical drive waveform, but this is simply due to the frequency response of the transducer (a loudspeaker) used in the experiment. In other words, the measurement is in itself a diagnostic of the transducer.

Note that the reconstruction calculation has no upper limit of dynamic range, i. e. works for any amplitude, and that, if preferred, in place of analog circuits, we could make the processing numerically, with a PC using an ADC for signal acquisition.

The reason for not being able to duplicate the same arrangement with a laser diode is because it appears very difficult to create two orthogonal modes at slightly different frequencies, very stable, and easily split.

The HeNe reconstruction will be used later for biosignal pickup (Sect. 5).

3.3. Velocity measurements

Basically, there are two versions of an SMI velocimeter, according to whether we wish to measure the *longitudinal* component of $\underline{\mathrm{v}}$, i. e. that $\mathrm{v}_{\|k}$ parallel to the wavevector $\underline{k}$ (or, more generally, to line-of-sight), or the *transversal* component $\mathrm{v}_{\perp k}$ (perpendicular to $\underline{k}$ or to line-of-sight).

In the first case, we may start by noting that the phase $2ks$ is actually written, in a more general form, as $\varphi = 2\underline{k} \bullet \underline{s}$, where the dot stands for the scalar product of vectors $\underline{k}$ and $\underline{s}$.

Then, as velocity is $\underline{\mathrm{v}} = d\underline{s}/dt$, by differentiating φ with respect to time we have $(d/dt)2\underline{k} \bullet \underline{s} = 2\underline{k} \bullet \underline{\mathrm{v}} = d\varphi/dt = \omega$. This equation simply tells us that the SMI output signal I_{ph} already contains the desired velocity component along the line-of-sight identified by the wavevector k, i. e. $\underline{k} \bullet \underline{\mathrm{v}} = \mathrm{v}_{\|k}$, and that the velocity $\mathrm{v}_{\|k}$ can be measured by the frequency $f = \omega 2\pi$ contained in signal I_{ph}, with a scale factor $2k/2\pi = 2/\lambda$. This is sometimes called the Doppler signal, yet it is nothing more than an interferometric phase-shift.

Thus, the measurement of longitudinal velocity is simply a byproduct of the normal SMI working principle, and several variants of the basic SMI concept have been discussed by Scalise et al [32]. A special feature is that, if the transversal component is negligible, the target spot remains the same during the movement and thus speckle statistics does not affect the measurement.

In the case of transversal velocity component, being $2\underline{k} \bullet \underline{\mathrm{v}} = 0$, we shouldn't observe any signal out of the SMI.

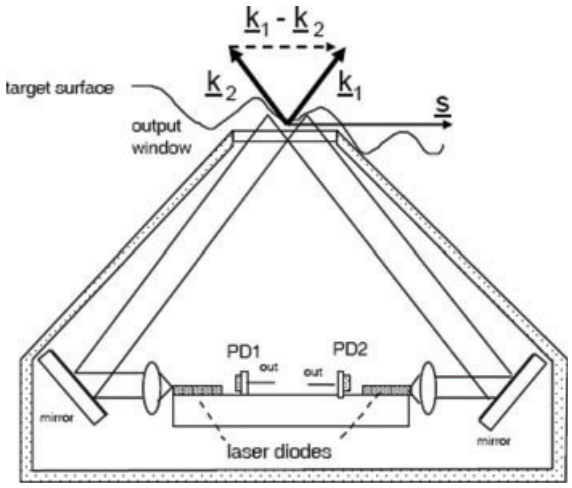

Figure 17 Application to scroll-sensing calls for a transversal velocity measurement. To detect $\mathrm{v}_{\perp} = d\underline{s}/dt$, a twin SMI arrangement is used, and the time derivative of the phase difference $\varphi_1 - \varphi_2$ is calculated, obtaining $2(\underline{k}_1 - \underline{k}_2) \bullet \underline{\mathrm{v}}$.

Yet something, depending on the velocity, is observed because, while the true interferometric signal is absent, the speckle statistics affects the otherwise constant field sent back into the laser, and generates a random-like modulated output current I_{ph}. The frequency content of I_{ph} can be correlated to the transversal component of velocity $\mathrm{v}_{\perp k}$ through an ad-hoc calibration [33], yet a velocimeter based on this principle has a somewhat erratic behavior also depending on the texture of the target surface.

A better configuration of a transversal-component velocimeter based on a true (SMI) interferometric signal can be developed by using a differential setup like the one illustrated in Fig. 17, used for sensing applications [34] (see also Sect. 6). If the wavevectors of the two separate (and nominally identical) SMI are $\underline{k}_1$ and $\underline{k}_2$, then we have the two output signals $\varphi_1 = 2\underline{k}_1 \bullet \underline{s}$ and $\varphi_2 = 2\underline{k}_2 \bullet \underline{s}$. Now, taking the difference of the phase signals measured by the SMIs, we get $\varphi_1 - \varphi_2 = 2(\underline{k}_1 - \underline{k}_2) \bullet \underline{s}$. Thus, the component sensed by signal $\varphi_1 - \varphi_2$ is oriented parallel to $\underline{k}_1 - \underline{k}_2$, which is transversal to the line of sight (Fig. 17).

Note that speckle statistics interferes also in this case with the SMI signal, but less seriously because the common-mode fluctuations are canceled out in the difference, and just a residual amplitude modulation due to diffuser sample changes is left, which can be made negligible by automatic gain control (ACG).

3.4. Distance measurements

Like any other interferometer, SMI is based on a phase-sensing mechanism, and thus multi-2π (or multi-λ) operation requires counting of phase increments, as seen in Sect. 3.1. Actually, we do not measure distance to a target, rather a displacement with an incremental accumulation of small steps (e. g., $\lambda/2$), and to do so we need to move the

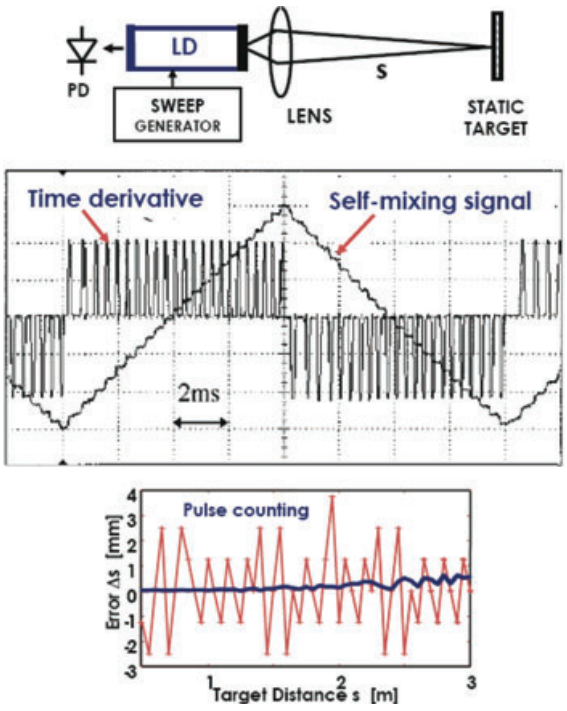

Figure 18 (online color at: www.lpr-journal.org) Distance measurement with a SMI: by a bias current sweep applied to the laser diode, wavelength is modulated with a triangular waveform, and phase $\varphi = 2ks$ exhibits a number N of 2π-periods variations (the small ripple on waveform). The SMI signal is time-differentiated and the periods N counted. Unit of scale distance is $\lambda^2/2\Delta\lambda$ and accordingly distance is $s = N\lambda^2/2\Delta\lambda$. Diagram at bottom is the spread of measurements on a $s = 1 \ldots 3$-m distance.

retroreflector from the $z = 0$ to the $z = s$ position and count the incremental steps.

This circumstance looks like precluding a true distance measurement with a phase-sensitive instrument like the interferometer. To overcome this limitation, Gouaux et al [35] proposed to take advantage of the dependence of the wavelength of emission from the bias current I_{bias} and sort out s from the phase $\varphi = 2ks$ (mod. 2π).

To this end, we impress a linear sweep to the bias current, of amplitude ΔI_{bias} (from a minimum I_0 to a maximum $I_0 + \Delta I_{\text{bias}}$) see Fig. 18. If $\alpha_\lambda = d\lambda/dI$ is the current-to-wavelength coefficient, the wavelength swing is $\Delta\lambda = \alpha_\lambda \Delta I_b$, and wave number k varies by $\Delta k = (2\pi/\lambda^2)\Delta\lambda$ accordingly [33, 35, 36]. For a still target ($s = \text{const.}$), we observe a variation of the optical phaseshift the SMI, given by $\Delta\varphi = 2s(2\pi/\lambda^2)\Delta\lambda$.

Dividing by 2π, we get the number of periods the interferometric signal of the SMI has passed through, or $N = 2s\Delta\lambda/\lambda^2$. From this equation we solve for s and obtain

$$s = N\lambda^2/2\Delta\lambda\,. \tag{13}$$

So, the procedure for an *absolute* distance measurement (as opposed to incremental) is to sweep the bias current to obtain a substantial $\Delta\lambda$, then count the periods N of the self-mixing signal during the sweep time, and find distance s using Eq. (13) [35, 36].

With regard to resolution, as Eq. (13) tells us, the unit of distance measurement is the factor multiplying N, or $d_{\text{unit}} = \lambda^2/2\Delta\lambda$. Then, we prefer to have a large $\Delta\lambda$ swing for best resolution, and commonly used laser Fabry-Perot laser diodes may have $\Delta\lambda = 0.1$ nm ($@\lambda = 0.85\,\mu$m), as limited by mode-hopping problems, resulting in a reasonable $d_{\text{unit}} = 3.6$ mm.

Figure 18 depicts the waveforms obtained in the SMI distance measuring instrument, and an example of repeatability of the measurement on a 1–3-m distance.

3.5. Angle measurements

Since the early times of SMI it has been observed that a reflection back into the laser from a remote mirror was readily detectable, because microphonics-induced vibrations collected from the ambient produce a sizeable SMI signal. The circumstance was used by Matsumoto [37] to align a HeNe infrared laser to an external remote mirror, down to $\alpha \approx 3$ arcsec angular resolution.

An improved version of the setup has been developed in [38] resulting in a true angle-measuring instrument, with performance comparable to a good optical autocollimator. The SMI setup (Fig. 19) uses a PZT-driven translation stage mounting the small objective lens of the laser diode, to modulate the aiming angle α and hence of the response signal I_{ph}.

As a well-known technique, commonly employed in instrumentation to find the condition of maximum response with the best accuracy, we look here at the phase relationship of the I_{ph} signal and compare it to the PZT drive. The arrangement is equivalent to transforming the nearly quadratic response of the plain SMI signal versus α into an almost linear one, with a zero crossing at the $\alpha = 0$ condition of best alignment (Fig. 19, bottom right). With conventional components, noise-limited resolution of ≈ 0.2 arcsec and dynamic range up to ≈ 5 arcmin have been demonstrated [38].

4. SMI measurement of laser parameters

Looking to the SMI signal waveform and to the fine features we can recognize in it, we realize they are not incidental, but are somehow related to physical parameters of the source. In particular, the jitter of the waveform switching at $C > 1$ unveils details about the laser linewidth, whereas waveform distortion and switching positioning at $C > 1$ are characteristic of parameters C, coupling strength, and α, the linewidth enhancement factor. In the following, we outline the principles of these two measurements based on waveform analysis.

4.1. Measurement of the laser linewidth

In the self-mixing signal, phase fluctuations of the step-down switching, revealed as a jitter of the waveform in

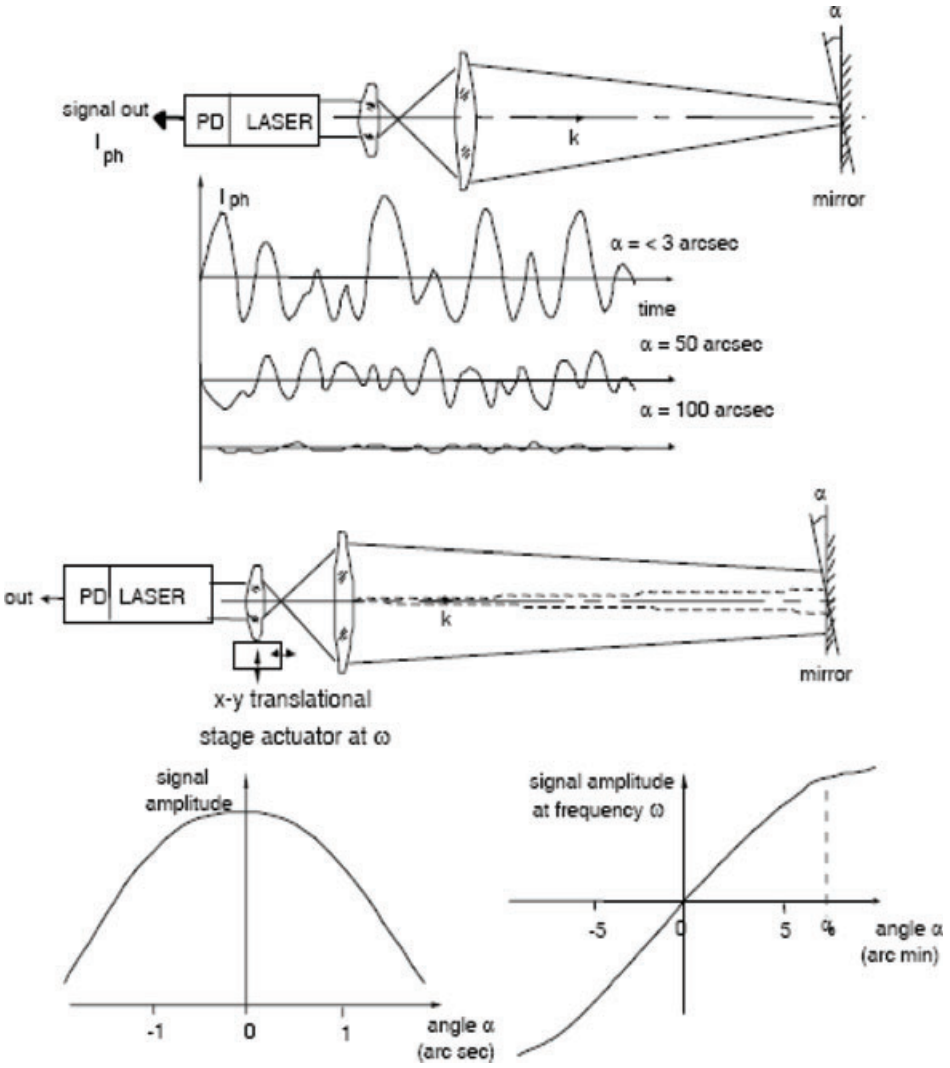

Figure 19 Alignment and angle measurement with a SMI: when a remote mirror is well aligned, the SMI signal due to ambient microphonics is maximized (top). In an improved setup, we modulate the angle by an XY piezo actuator slightly moving the objective lens. The resulting SMI signal is sensed in amplitude and phase respect to the drive signal (+/− sign for phase/antiphase). The parabolic-like response curve (lower left) is thus transformed in a quasi-linear passing through the zero. Angles down to a fraction of arc-sec can be measured on a dynamic range of a few arc-min (adapted from [38]).

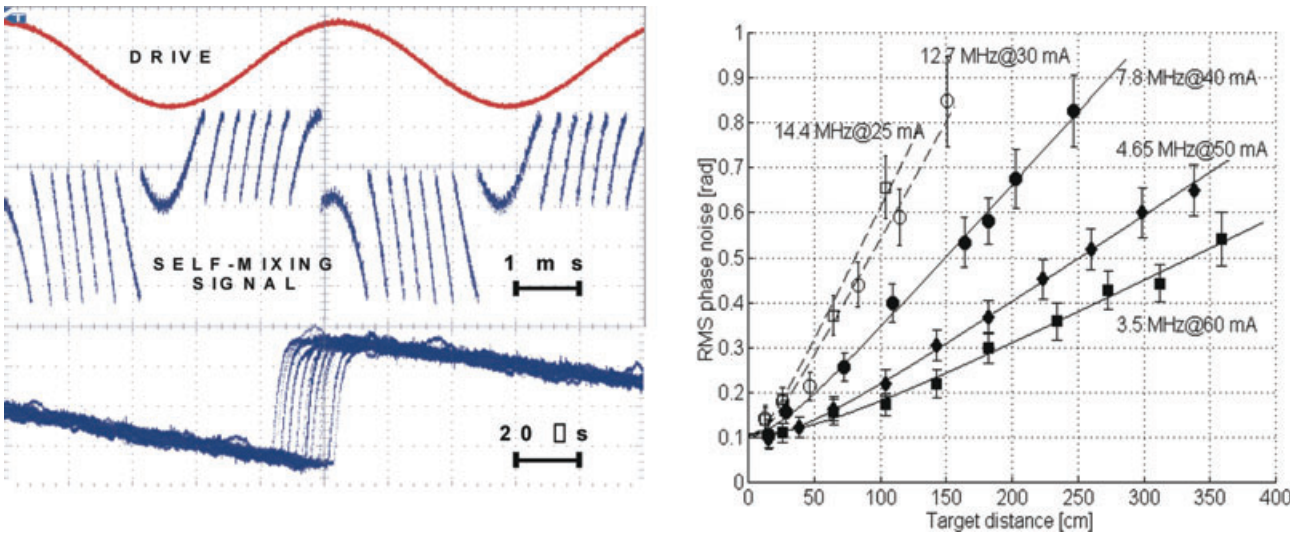

Figure 20 (online color at: www.lpr-journal.org) Linewidth measurement by SMI: the laser is set to a $C > 1$ regime and we look at the jitter of the switching transient appearing in the self-mixing waveform (bottom left). The variance of the associated phase fluctuation $\Delta 2ks = 2k\Delta s + 2s\Delta k$, has a first term which is kept constant, and a second term $2s\Delta\nu/c$ proportional to the linewidth $\Delta\nu$. At right, the quadratic sum of variance contributions is fitted to obtain the linewidths of different laser specimen (from [39], courtesy of the IEEE).

Fig. 20 (lower left), are caused either by a small variation ΔL of target displacement, $s = L_0 + \Delta L$, or by a variation of wavevector $\Delta k = \Delta\nu/c$ around $k_0 = 2\pi\nu_0/c$. As pointed out by Giuliani and Norgia [39], the two contributions (statistically independent) add to the phase variance $\langle\varphi^2\rangle$ and are easily written as:

$$\begin{aligned}\Delta\langle\varphi^2\rangle &= \Delta\langle(2ks)^2\rangle \\ &= 4\left[k_0^2\langle\Delta L^2\rangle + L_0^2\langle\Delta k^2\rangle\right] \\ &= (4\pi/c)^2\left[\nu_0^2\langle\Delta L^2\rangle + L_0^2\langle\Delta\nu^2\rangle\right]. \end{aligned} \tag{14}$$

Now, applying a sawtooth drive to ΔL, we can measure the total phase variance $\Delta\langle\varphi^2\rangle$ and fit it to a line $L_0^2\langle\Delta\nu^2\rangle +$ const., where the constant term is $(4\pi/c)^2\nu_0^2\langle\Delta L^2\rangle$.

The results are shown in Fig. 20. We apply a small (few λs) drive signal to a retroreflector, positioned at $L_0 = 10$ cm to 3.5 m, and get a small added constant term (= 0.1 rad). Superposed quadratically to it, as given by Eq. (14), we find the desired linewidth term $L_0^2\langle\Delta\nu^2\rangle$ which is then easily measured with a few steps of 50-cm increment in L_0.

As we can see from Fig. 20, with a displacement of a few meters we can measure linewidths $\Delta\nu$ ranging from 3.5 to 14 MHz, and the minimum measurable linewidth is estimated ≈ 1 MHz. Given this limit, we conclude that the method requires much less lab space that the usual measurement method based on arm mismatch (also called delayed heterodyne) requiring a propagation length of the order of $c/\Delta\nu \approx 300$ m for 1 MHz.

Note that the linewidth measured in the self-mixing regime might be different from the unperturbed one. Luckily, at the switching time where the measurement is done, the phase of feedback is $\pi/2$ and the linewidth is unaffected by feedback, as calculated by Petermann in [14].

Finally, let us note that the method also gives the coherence length as $L_c = c/\sqrt{\langle\Delta\nu^2\rangle}$, again requiring an external arm length $L_0 \ll L_c$ much less than the coherence length.

4.2. Measurement of the alfa factor

The waveform $F(\varphi) = \cos\omega\tau$ of the SMI signal depends primarily on the feedback factor C and also, to a minor extent, on the linewidth enhancement factor or alfa factor α as indicated by Eq. (4d).

Several different parameters can be chosen to describe the F waveshape and its dependence on α and C. We need at least two of them to invert their functional dependence and find α and C.

In general, the most suitable parameters should: (i) sharply depend on α and C, (ii) be possibly orthogonal (to ease the functional inversion), and (iii) be easily measured with good accuracy from waveform $F(\varphi)$ (also at moderate SNR).

As proposed by Yu et al [40], a satisfactory choice is a pair of phase delays, for example φ_{13}, from upgoing zero crossing to downgoing switching, and φ_{24}, from downgoing zero crossing to upgoing switching, see Fig. 21 (left). From Eq. (4d), we find the following expressions for these phase terms as [40]:

$$\begin{aligned}\varphi_{13} &= \sqrt{(C^2-1)} + C/\sqrt{(1+\alpha^2)} + \arccos(-1/C) \\ &\quad - \arctan\alpha + \pi/2, \\ \varphi_{24} &= \sqrt{(C^2-1)} - C/\sqrt{(1+\alpha^2)} + \arccos(-1/C) \\ &\quad + \arctan\alpha - \pi/2. \end{aligned} \tag{15}$$

In Fig. 21 (right) we plot the diagram of the dependence of $X_{13} = \varphi_1/2\pi$ and of $X_{24} = \varphi_2/2\pi$ from C and α.

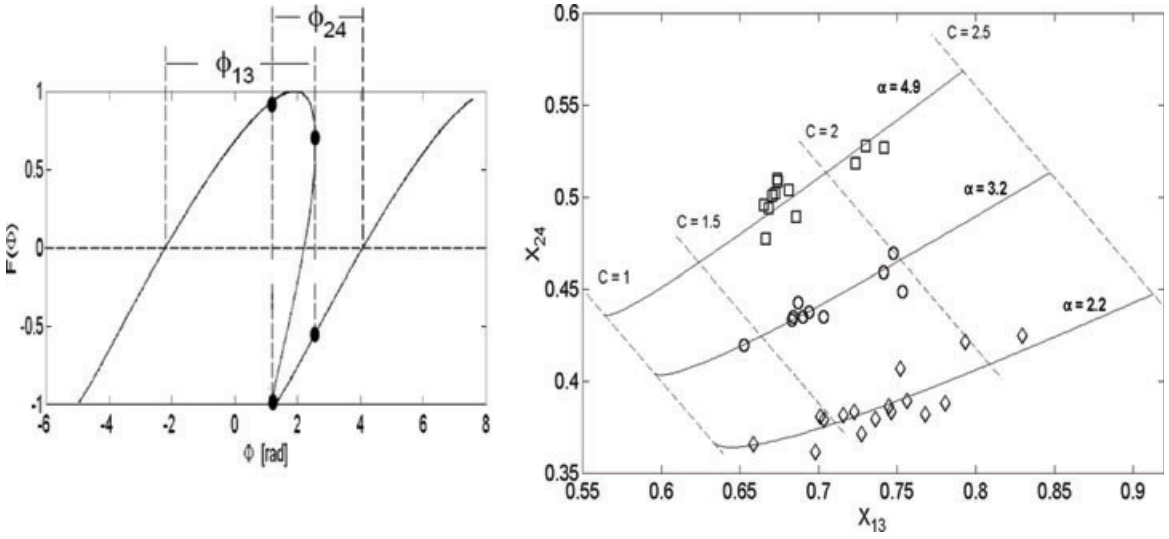

Figure 21 Alfa factor measurement: details of the waveform of $F(\varphi)$ depends on parameters α and C of Adler's equation. We choose the phase delays from zero crossing to downgoing switching, φ_{13}, and from zero crossing to upgoing switching, φ_{24} (left). With the aid of Eq. (9), we calculate the dependence of $X_{13} = \varphi_{13}/\pi$ and $X_{24} = \varphi_{24}/\pi$ from C and α and plot the diagram at right. Now, when we measure a pair of values X_{13} and X_{24}, we identify a point in the diagram and can read the corresponding C and α values (from [40], courtesy of the IEEE).

Once the values of φ_{13} and φ_2 have been measured on a waveform, we can report them in the diagram of Fig. 21 and obtain α and C, via a graphical solution of the parameter equation (Eq. (15)).

In Fig. 21 several experimental points are reported for different laser diodes. Note that the α factor measurement process also supplies the C factor at the same time. The C factor is, however, a parameter describing the setup, not the device or the laser source.

Of course, Eq. (15) and Fig. 21 are applicable for $C > 1$ only, because they are based on switching times (or phases).

Yet, for $C < 1$ other parameters can be easily found out, similar to those of Eq. (15) or Eq. (12), as already mentioned.

Another issue with the α factor measurement concerns the accuracy of the experimental determination. Xi et al. [41] proposed to fit directly the $F(\varphi)$ waveform with an analytical expression (like e. g., Eq. (11)) where C and α are free parameters and apply a minimization algorithm based on a cost function. The estimated accuracy of the α factor, evaluated by a test of self-consistency, is $\approx 6.5\%$ using the above noted phases φ_{13} and φ_{24}, and may go down to 2–4% with more sophisticated methods [41].

A final point worth a comment is on the importance of the α factor. Actually, the α is not a true physical parameter of the laser, rather it is an ad-hoc parameter introduced in the L-K equations (Eq. (5)) to justify the excess linewidth. The introduction is successful because α values are self-consistent in adjusting the performance evaluation and fit a class of same-type experiments. Yet, when a round-robin measurement of α factor was carried out by Villafranca et al [42] to compare the α from several different measurement methods, a disappointingly large spread was found. A possible explanation is that several elemental contributions to the α factor [43] have different weights in different applications – thus justifying a large spread. In conclusion, clarifying the meaning of the α factor is still an open issue.

5. SMI measurement of physical quantities

In the following we describe several different physical quantities that can be measured with SMI, taking advantage of the simplicity of the SMI setup and of its special features.

5.1. SMI measurement of thickness and refraction index

A frequently used configuration to measure the thickness of a transparent slab is a shear interferometer, in which the direct beam of the laser is superposed on the photodetector (PD2) to the beam double-reflected at the slab walls (see Fig. 22, left). This generates an interferometric signal of the type:

$$\Delta\varphi_{PD2} = 2knd\cos\theta\,, \tag{16a}$$

here, phase is dependent on both the thickness d and the index of refraction n of the slab, as normally found in optical pathlength measurements. We can also get another interferometer signal at PD1 (Fig. 22), a self-mixing signal generated by the beam going through the slab, down to photodiode PD2 and back, retracing the optical path up to the source. The second phase signal at photodiode PD1, a true SMI signal, is:

$$\Delta\varphi_{PD1} = 2kd(n\cos\theta - \cos\alpha)\,. \tag{16b}$$

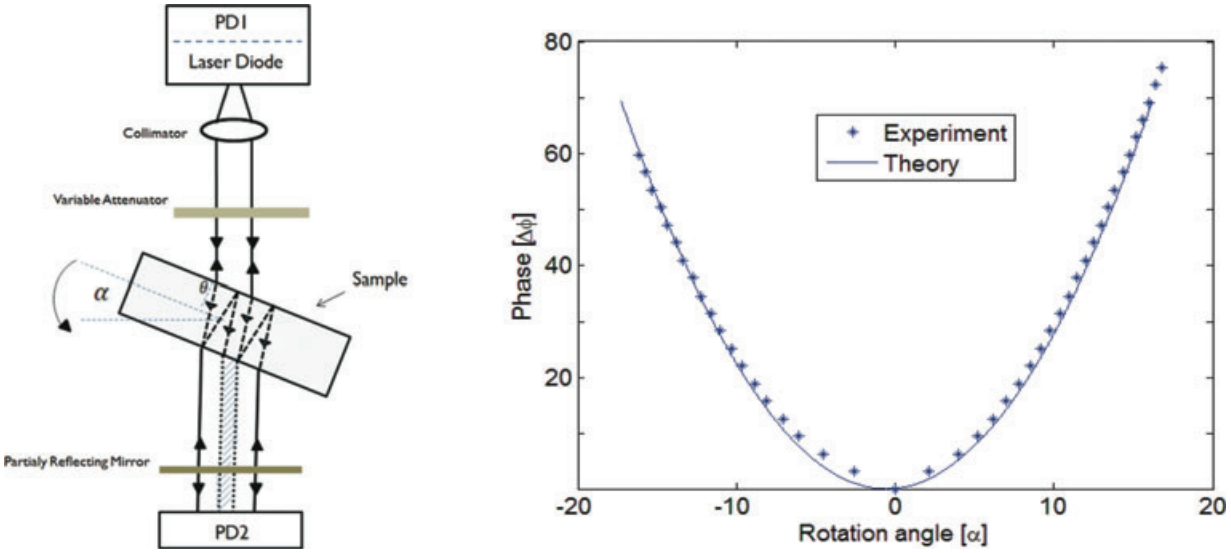

Figure 22 (online color at: www.lpr-journal.org) Transparent slab thickness measurement with SMI: (left) a laser diode acts as a self-mixing sensor (output on photodiode PD1) and as a source of a lateral shear interferometer (output on photodiode PD2). Subtraction of the fringes of the two outputs yields $kd\cos\alpha$, function of tilt angle α (right) and independent from n. Range of thickness is measured from ≈ 5 to 1000 µm (adapted from [44]).

By subtracting the two phases of Eqs. (16a and b), we have obtained [43]:

$$\Delta\varphi = \Delta\varphi_{PD2} - \Delta\varphi_{PD1} = 2kd\cos\alpha \qquad (16c)$$

and the result is no longer dependent on n. On rotating the slab (the angle α was turned from -30 to $+30$ deg, typically) the shear and SMI waveforms were measured and, after a scale adjustment $\Delta\varphi$ was computed and Eq. (16c) solved for d in units of $2\pi/2k = \lambda/2$.

The range of measurement was typically is 5–2000 µm, and the accuracy $\approx 2\%$ [44]. In principle, once d is measured, we can go back to the PD2 signal (Eq. (16a)) and also solve for the index of refraction.

5.2. SMI measurement of roughness

Backscatter from a rough surface carries information on surface texture and rms height roughness. A few papers describing the properties of the SMI signal obtained as a surface echo and associated processing have been reported, see e. g. [45, 46]

5.3. SMI measurement of mechanical resonance

In some SMI measurements, we can take advantage of knowing the drive waveform $s(t)$, like in the case of detecting mechanical resonance in a MEMS, and be able to greatly simplify signal handling.

As we can see in Fig. 23, we measure the inplane movement of the spring-suspended test mass of a gyroscope MEMS [47, 48] by aiming an SMI laser beam at a slant angle (for example, 20 deg), so as to get a sizeable $2\underline{k} \bullet \underline{s}$. The typical test mass is a square slab of Si, a fraction of mm on a side, with many holes etched in it to remove weight (so as to have a high resonant frequency).

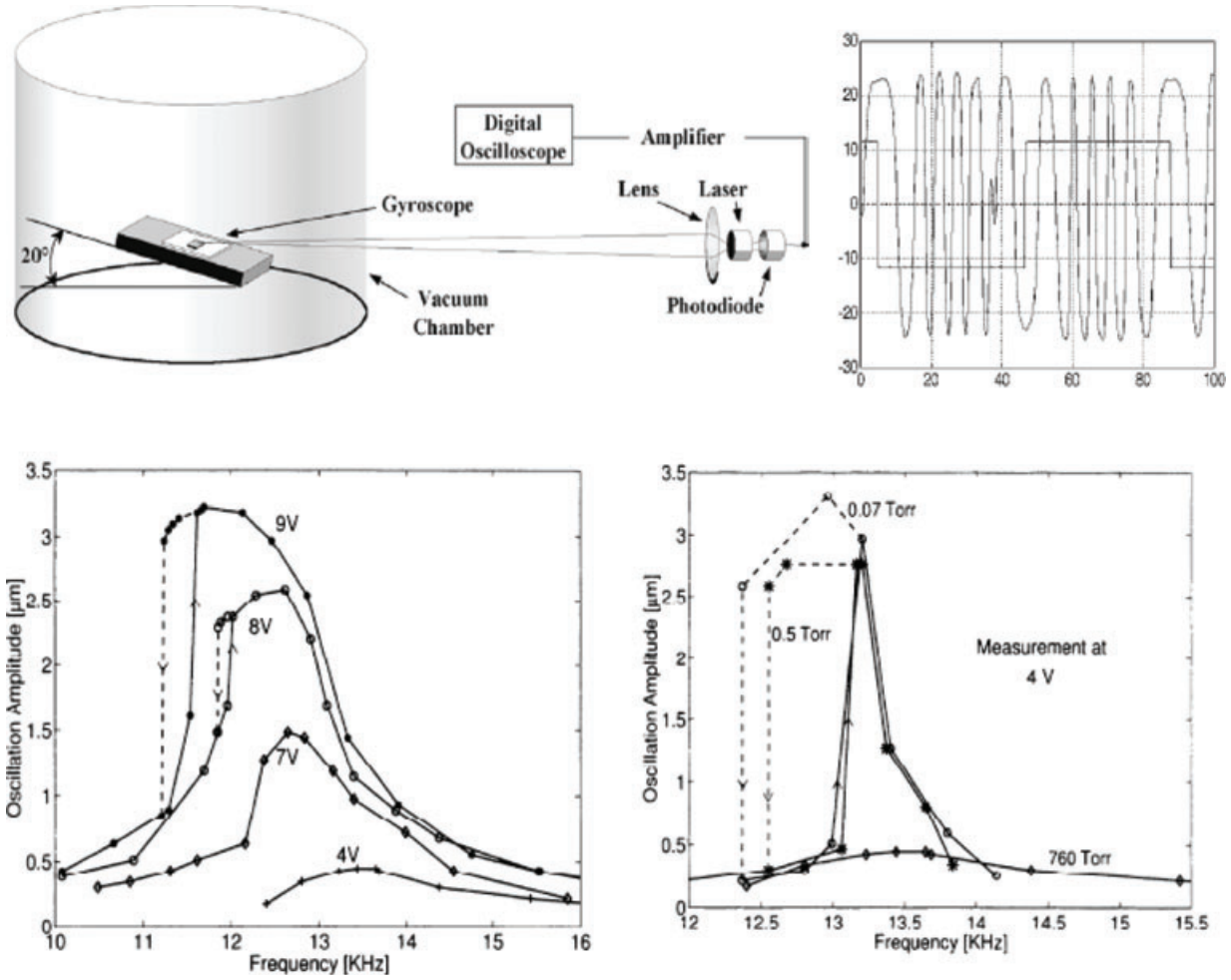

Figure 23 To test the mechanical properties of Si-machined MEMS with SMI, light from the laser (top left) is focused on the small vibrating mass of the chip through the glass wall of a vacuum chamber. The vibration of the mass is viewed at an angle ($\approx 20°$), and the appropriate correction is appied to the SMI fringe signal (top right) giving the displacement waveform. Bottom left: as drive voltage is increased, we find a drift of resonant frequency and then hysteresis shows up at 8. . . 9 V, indicating incipient fatigue and creep. Bottom right: at increasing chamber pressure, the Q-factor of resonance is damped because of residual air friction (from [47], courtesy of the IEEE).

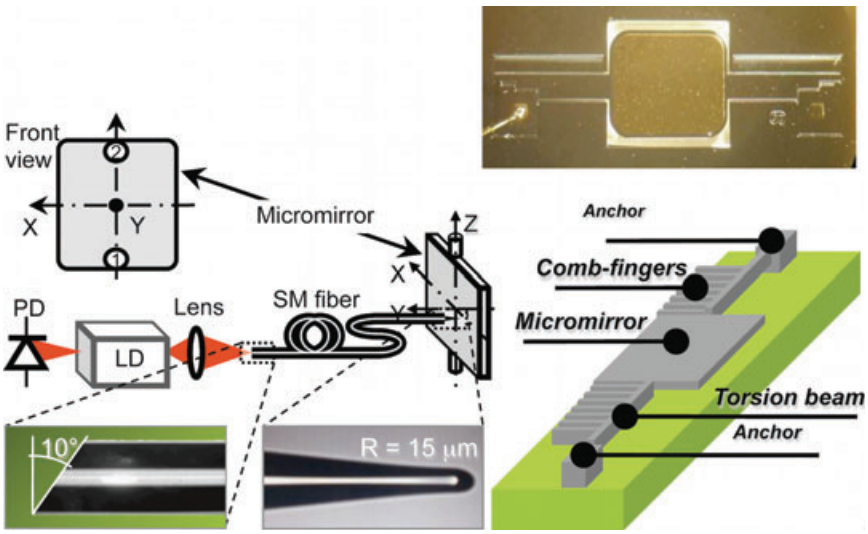

Figure 24 (online color at: www.lpr-journal.org) Small micromirrors of a Si-machined MEMS can be tested by using a single mode fiber as the probe pinpointing the mirror. The fiber has a tilted splice at the laser chip coupling end, and is tapered and lensed at the other end to sense the mirror movement (adapted from [48], courtesy of the IEEE).

The surface of the mass appears optically rough. The SMI is well suited for this uneasy measurement because it works on a diffuser target as well, is not disturbed by light falling on still parts or outside the target, and wavefront distortion of the (non-optical finish) walls of the vacuum-tight enclosure is no problem.

To measure the mechanical response, we drive the MEMS exciting comb structure by a square-wave excitation V_{exc} and measure the amplitude of the corresponding displacement.

Knowing where the V_{exc} starts and ends, it is an easy matter to count periods of the interferometric signal, that is, measure the amplitude in $\lambda/2$ steps (and fractions of it). Thus, we can plot a frequency-response diagram for the MEMS (Fig. 23) with the drive voltage V_{exc} as a parameter. In the diagram, hysteresis of the response curve reveals incipient fatigue and creep of the mechanical structure, a very crucial point in MEMS design, given that Si is very well known as an electronic material but much less is known of its mechanical properties, especially at high stress levels. The same measurement, as a function of pressure, reveals the practical damping factor of the mechanical Q, a parameter not easily calculated.

Another sensing of a MEMS structure, the micromirror of a photonic switching device, has been carried out by Annovazzi et al [48] with the aid of an SMI setup modified with the insertion of a fiber pigtail (Fig. 24), tapered and lensed at the target end to pinpoint the small micromirror, so as to detect its response to excitation and resonance frequency.

5.4. SMI measurement of stress/strain hysteresis

The SMI vibrometer described in Sect. 3.2.1 was developed further with the addition of the differential mode of operation, to be able to measure small vibrations superposed onto larger common-mode movements.

To make a differential measurement with conventional configurations of an interferometer, we take advantage of the usually available reference arm, so that we measure $\varphi_1 - \varphi_2 = 2k(s_1 - s_2)$. Yet, if we want to work on a diffuser-like target surface, the speckle statistics will impair the phase difference, adding a large error-phase term φ_{sp}.

Using the SMI half-fringe stabilized vibrometer with the phase signal internal to the feedback loop, we have removed the error φ_{sp}, as explained in Sect. 3.2.1, yet we lack a second reference (optical) arm for the differential measurement.

We can subtract electrical signals, however, and make a double-channel SMI vibrometer, with one channel aimed to the common mode signal s_{CM}, and the other aimed to $s_{CM} + s_D$, containing the differential signal s_D.

After checking that two channels can be built with nearly identical performance (mismatch in responsivity $< 0.1\%$, noise floor and dynamic range differing by $< 5\%$) [49], we concluded that the electronic subtraction differential behaves as well as the optical phase differential interferometer and deployed it in a mechanical test application.

The experiment was a brake-bead testbed (see Fig. 25) in which a shaker stresses into vibration a bead onto a break support. The stress is a quasisinusoid V_{ST} excitation, and the support vibration is the s_{CM}, while the bead vibration is the differential s_D. The common mode is about 15–30 μm wide, and the differential is 0.5–4 μm.

From the mechanics point of view, the V_{ST} excitation is proportional to the stress T, and the differential s_D is proportional to the strain S of our mechanical sample.

With the (electronic) differential SMI, we were able to measure [49] the hysteresis T-S diagram of our sample, for the first time to the best of our knowledge. As we can see from the result reported in Fig. 26, at moderate stress the sample is in the elastic or Newtonian regime, with a linear dependence of S on T and no hysteresis. At a certain threshold, the material enters the plastic regime and the diagram opens up with hysteresis. The hysteresis cycle widens until, on a little further increase in T, the sample breaks down (and the curve disappears).

Of course, the above information is of great value for the design and testing of mechanical structures. In this application, the SMI vibrometer is the key instrument to measure it.

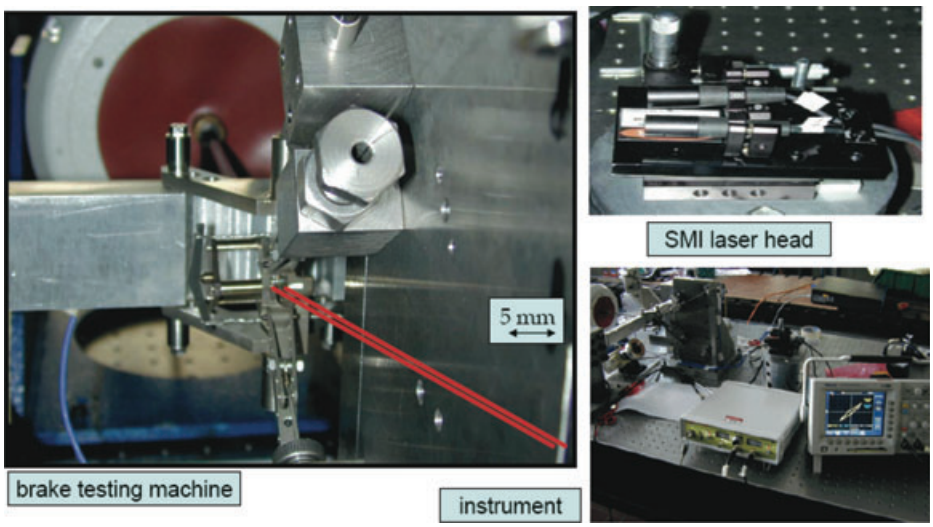

Figure 25 (online color at: www.lpr-journal.org) The SMI half-fringe servoed vibrometer can also work in differential mode on a diffuser target, here the damper bead of a turbine motor brake. The two (red) beams point at the base of the shaker (common mode) and the bead body (measurement) (courtesy of M. M.Gola, Polytechnic of Turin, Italy)

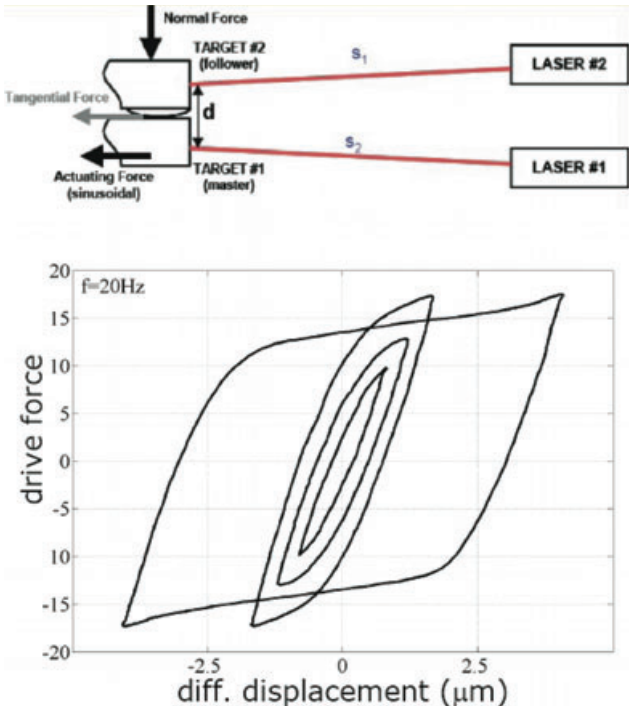

Figure 26 (online color at: www.lpr-journal.org) The Strain-Stress diagram is measured optically for the first time with the SMI differential vibrometer, and reveals the Newtonian regime where hysteresis is negligible ($F < 7$ N), and the plastic regime where the hysteresis loop opens ($F = 8 \ldots 15$ N) and the bead dissipates energy, before the breakdown occurrs (at $F \cong 17.5$ N).

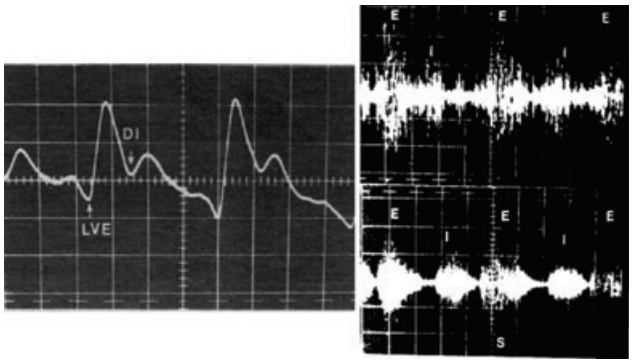

Figure 27 Two samples of biomedical signals measured by the He-Ne SMI (see also Sect. 3.2.3) left: pulsation of blood on a finger tip (0.5 μm/div, 0.3 s/div), right: respiratory sounds detected on the back of a patient, with the acoustical signal of a stethoscope (top right) compared to optical waveform taken by SMI (bottom right)

5.5. SMI measurement of biological motility

The sin/cos reconstruction vibrometer (Section 3.2.3) has been used to pick up several kind of signals of biological origin [50].

In a clinical experiment in cardiology, the heart-beat pulsation on the finger tip of a normal subject was observed, replicating the shape of the cardiac pulsation, and exhibiting details well known to the cardiologist, like the LVE (left ventricular ejection) and DI (dichrotic incisure), usually found in the normal ECG (Fig. 27).

Using another SMI arrangement, Hast et al [51] conducted a survey on a sample of 200 volunteers, measuring the Doppler signal ($d\varphi/dt = 2kv$) of the cardiovascolar pulse in radial arteries of the forearm. They found $d\varphi/dt$ is well correlated ($c = 0.84$) to the time derivative of the blood-pressure waveform taken on the middle finger. This is an important result confirming the validity of diagnostics made by SMI.

The sin/cos vibrometer was able to pick up [50] respiratory sounds on the back of a live subject. Inspiration and expiration noises (I and E in Fig. 27) were clearly measured, finding waveforms similar to those of the traditional acoustical stethoscope, except for missing spikes (Fig. 27 right), identified as artifacts due to skin friction under the stethoscope during respiration.

In all experiments of motility pickup on the skin, surfaces were untreated, yet the patient had to be immobilized to avoid corruption of SMI signals because of the speckle pattern statistics.

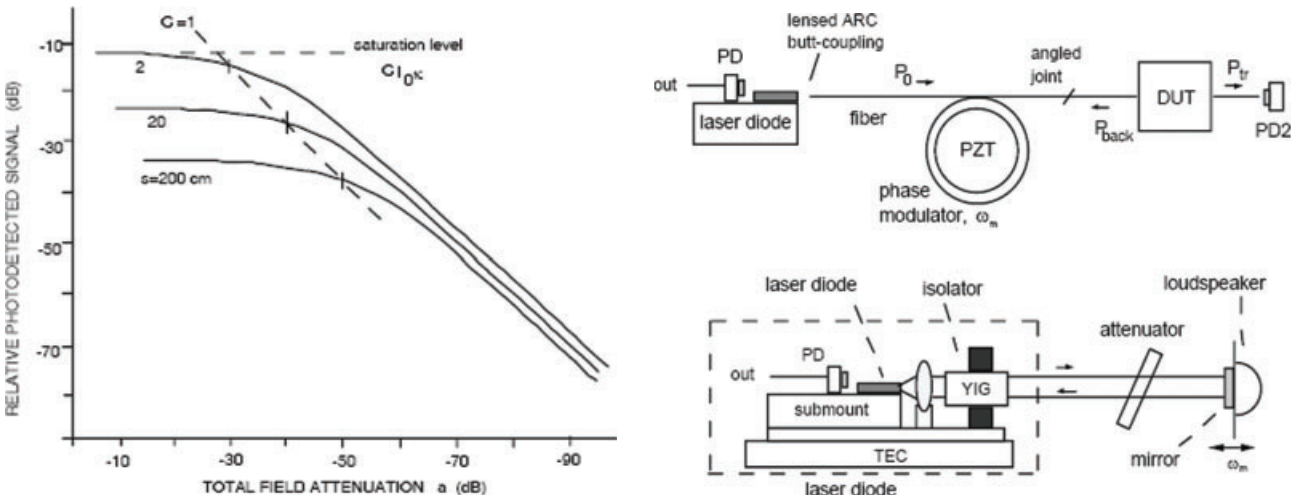

Figure 28 As an echo detector, the SMI can sense returns as small as 10^{-9} of the output power (left). To measure the return loss or the isolation loss, (right) we add a modulation of the pathlength at a carrier frequency ω_0, through an coiled PZT phase-modulator or a target-end loudspeaker. The SMI signal output is then read at frequency ω_0. Its amplitude provides the return loss of the DUT or the insertion loss of the isolator.

An interesting application to biological signal pickup was recently reported by Rovati et al [52]. With a superluminescent diode as the source of the SMI, they were able to measure the velocity profile of a liquid flow in a vein-simulating capillary tube. Pesatori et al [53] reported an improved version of the SMI aimed at blood-flow measurement, where the capillary is aimed axially at a slant angle θ to develop a signal $2ks' \cos\theta$.

Taking advantage of the shorter emission wavelength of a GaN, $\lambda = 405$ nm, and using a slant angle $\theta = 15$ deg to look at a capillary tube, Kliese et al [54] were able to report a minimum measurable flow velocity as low as 26 µm/s.

6. SMI applications to sensing

Applications to *sensing* is when an SMI is used to measure amplitudes of incoming signals, as opposed to phase measurements considered till now. As pointed out in Sect. 2, the SMI scheme belongs to the class of coherent detectors [4] giving an output proportional to the *field* amplitude, and characterized by the operation always in the desirable regime of quantum limit of detection, i. e. with the SNR limited by the quantization (or granularity) of the incoming photon flux.

So, the ability of SMI to sense very small signals with a high sensitivity is exploited in several applications.

6.1. SMI detection of remote echoes and return loss

The response of an SMI to remote echoes is easily characterized using a mirror and attenuator combination to let a fraction of emitted power re-enter the laser cavity [55]. The amplitude of the detected signal versus the attenuation suffered in the go-and-return path is plotted in the diagram of Fig. 28 for a typical laser diode (5 mW power, $\lambda = 825$ nm).

As we can see, the SMI can detect an echo as small as 10^{-9} of the output power, with a saturation at $\approx 10^{-3}$ as due to the intervening strong regime of injection ($C > 1$). The echo detector is thus a very sensitive return-loss measuring instrument (Fig. 28).

We can also make an in-situ measurement of the isolation factor of an optical isolator mounted in front of the laser chip to protect it from reflections [55, 56].

The only feature we need to add is a phase modulation of the optical path, so that the amplitude of the remote echo is moved from the zero-frequency component to a carrier ω_0 (the modulation frequency), making it easier to perform the amplitude measurement, away from low-frequency drifts.

As a component, the phase modulator may be either a piezoceramic-driven fiber coil for a guided-propagation version, or a loudspeaker for free space propagation.

In Fig. 28 (right) we report two schemes for the measurement of: (i) return-loss of a fiberoptic DUT (device under test), and (ii) isolation factor of an optical isolator mounted in front of the chip (a case that can't be covered by other approaches). In both cases, the reported sensitivity to returning power is better than 10^{-8} or -80 dB [55].

6.2. SMI application to confocal microscopy

The SMI sensor has also been applied to a confocal microscope arrangement. Following the proposal of Lu et al [57], the use of SMI permits a simplification of the alignment procedure of the optical setup (see Fig. 29).

While lateral resolution is of course the diffraction limit λ/πNA, the in-depth resolution can reach 30–50 nm thanks to the electronic processing of the SMI-detected signal [57].

Developing the concept further, Wang et al have proposed [58] a scanning profilometer, based on a SMI confocal microscope, capable of resolving 10 nm height on a sample 5 µm by side.

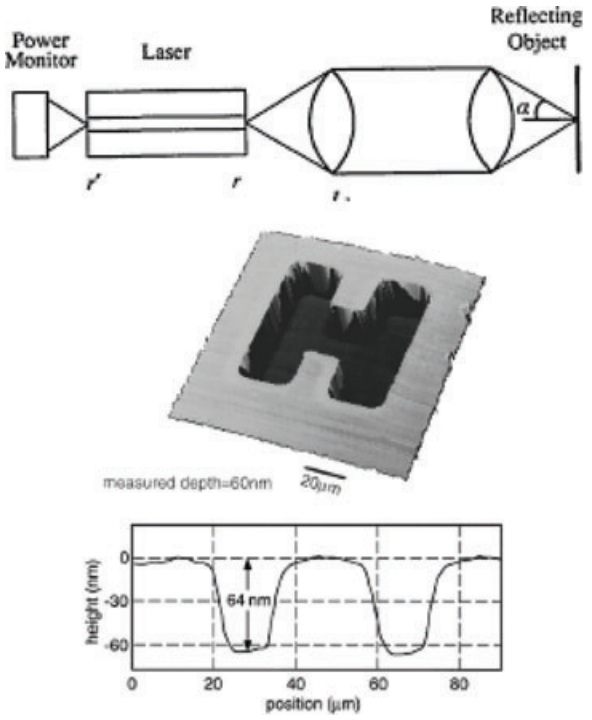

Figure 29 The SMI can be used in connection to a confocal microscope layout with the advantage of self-alignment of the detector. Scanning the specimen generates an image with a spatial resolution $r = \lambda/\pi \mathrm{NA} \approx 1$-μm and a typical depth resolution $\Delta z \approx 30$-nm (from [57] by courtesy of the OSA).

6.3. SMI application to scroll sensors and CD readout

The application of SMI to a scroll sensor has been already discussed in Sect. 3.3 and Fig. 17, as an example of transversal-component velocity sensor.

Another related consumer application, demonstrated by Ukita et al [59] is the readout of pits in the CD and DVD disk, illustrated in Fig. 30. The SMI is an echo sensor because unwritten portions of the disk surface reflect light and give a large signal, whereas pits diffuse light and give a small return.

With respect to a combination of laser and photodetector requiring a beamsplitter BS to combine the two paths, the SMI offers the advantage of a more compact setup [34, 59], and saves the use of the BS (but requires a monomode laser, in general).

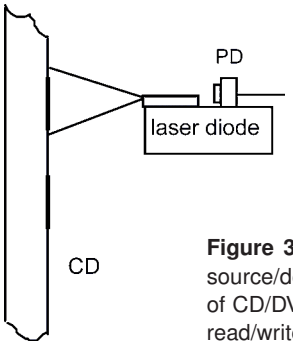

Figure 30 The SMI can be used as the source/detector combination in the readout of CD/DVD disk, as it simplifies the optical read/write layout.

7. Conclusions

In this paper we have presented an overview of instrumentation developed from the concept of self-mixing interferometry, an approach based on weak coupling phenomena in laser diodes. We have shown that SMI is conveniently applied not only to kinematics and dimensional-related measurements covered by traditional interferometry, but also to the measurements of physical parameters, to small-signal sensing, and echo detection.

We have also tried to systematize the field of SMI measurements, discussing several versions of SMI that differ on features like dynamic range, noise, periodic vs. aperiodic displacement, analog versus digital processing, etc., which are not only performance but actually represent different classes of instrument.

The examples reported in this paper inevitably reflect the scientific interest of the author and his group, yet they should hopefully be representative of basic ideas and tools we can deploy in research on SMI measurements.

In particular, rather than a list of contributions, we have tried to show the guiding principles underpinning the applications being developed, and how methods and options from different disciplines (electronics, communication, control theory, etc.) can cross-fertilize the SMI concepts, which really makes SMI an effective and sophisticated approach, quite different from the apparent simplicity of its basic setup.

Self-mixing is still far from being fully exploited, and we think that, in the years to come, it will continue to offer an excellent opportunity for the activity of young researchers and a ground to make the most of his/her creativity and talent.

Acknowledgements. The content of this paper is largely based on a Distinguished Lecture program awarded to the author by the IEEE Photonics (previously IEEE LEOS) Society, whose sponsorship is gratefully acknowledged. The author also wishes to acknowledge several people at the Department of Electronics of University of Pavia who have contributed to the researches described in the text and cited in the references, and in particular those who carried out their activity while being postdoc or PhD students of the ElectroOptics Group before they became Professors at the Faculty of Engineering: Guido Giuliani, Michele Norgia (now at Politecnico Milano), Sabina Merlo, Valerio Annovazzi-Lodi, Marc Sorel (now at Glasgow University), Alessandro Scire' (now at Universitat Illes Balears, Spain), Giuseppe Martini and Valeria Speziali, and also the former PhD and graduate students Davide d'Alessandro, Luca Falzoni, Marco Passerini, Simone Bozzi-Pietra, Luca Tizzoni, Enrico Randone, and Mohammad Taghi Fathi.

Received: 10 January 2011, **Revised:** 30 May 2011, **Accepted:** 3 June 2011

Published online: 13 September 2011

Key words: Optical instruments, interferometry, self-mixing, laser diodes.

Silvano Donati earned his Laurea degree in Physics in 1966 at the University of Milan. In 1980 he became Full Professor of Optoelectronics at the Department of Electronics in Pavia. He taught courses in electronic circuit design, electronics materials and technology, photodetector devices, electrooptical instrumentation and optical fiber communications. With the IEEE-LEOS he started workshops on fiberoptics passive components and optical distance measurements and applications before being passed on to IEEE Chapters in Glasgow, Palermo and Taipei, Madrid and Oulu. He was Visiting Professor at National Taiwan University in Taipei and at National Sun Yat Sen University in Kaohsiung. He is Life Fellow of the IEEE, Fellow of OSA, and Meritorious Member of AEIT. You may download his papers at his website http://www.unipv.it/donati, or propose/discuss ideas about research writing to him donati@unipv.it.

Note added in proof An interesting example of detection offered by the self-mixing scheme used as a coherent echo detector (Sect. 6.1) has been described in a recent paper by P. Dean et al [60]. The novelty respect to previously reported cases (as in [55] and Fig. 28) is the wavelength range of application – THz waves – and the readout using the voltage across the diode laser junction. Thus, the SMI works not only as the source of radiation to sense the remote target, but also as a detector of the weak returning signal, down to a demonstrated level of about −50 dBm, a remarkable result for a THz detectorless system.

References

[1] M. B. Spencer and W. E. Lamb, Phys. Rev. A **5**, 884–891 (1972).
[2] M. B. Spencer and W. E. Lamb, Phys. Rev. A **5**, 891–897 (1972).
[3] R. Lang and K. Kobayashi, IEEE J. Quantum Electron. **16**, 347–355 (1980).
[4] S. Donati, Photodetectors, (Prentice Hall, Upper Saddle River, NJ, 2000), Sect. 8.4.
[5] S. Donati, Electrooptical Instrumentation, (Prentice Hall, Upper Saddle River, NJ, 2004), Sect. 4.5.2.
[6] V. Annovazzi Lodi and S. Donati, IEEE J. Quantum Electron. **16**, 859–865 (1980).
[7] D. M. K. Kane and K. A. Shore, Unlocking Dynamic Diversity – Optical Feedback Effects on Semiconductor Lasers, (J. Wiley & Sons Ltd, London, 2008); K. Ohtsubo, Semiconductor Lasers: Stability, Instability and Chaos, Springer Series Optical Sciences 111, (Springer-Verlag, New York, 2006).
[8] S. Donati, G. Giuliani, and S. Merlo, IEEE J. Quantum Electron. **31**, 113–119 (1995).
[9] S. Donati, J. Appl. Phys. **49**, 495–497 (1978).
[10] S. Donati, Photodetectors, (Prentice Hall, Upper Saddle River, NJ, 2000), Sect. 8.1.
[11] G. A. Acket, D. Lenstra, A. J. DenBoef, and B. H. Verbek, IEEE J. Quantum Electron. **20**, 1163–1169 (1984).
[12] E. Randone and S. Donati, Opt. Exp. **14**, 9788–9796 (2006).
[13] W. M. Wang, K. T. W. Grattan, A. W. Palmer, and W. J. Boyle, IEEE J. Lightwave Technol. **12**, 1577–1587 (1994).
[14] K. Petermann, Laser Diode Modulation and Noise, (Kluwer Academic Publishers, Dordrecht, 1991).
[15] C. H. Henry, IEEE J. Lightwave Technol. **4**, 288–1297 (1986); M. Osinski, and J. Buus, IEEE J. Quantum Electron. **23**, 9–27 (1986).
[16] R. W. Tkach and A. R. Chraplyvy, J. Lightwave Technol. **4**, 1655–1661 (1986).
[17] S. Donati, Electrooptical Instrumentation, (Prentice Hall, Upper Saddle River, NJ, 2004), Chap. 4, pp. 89–180.
[18] A. F. Rudé and M. J. Ward, Hewlett-Packard J. **27**(6), 2–6 (1976).
[19] S. Donati, Electrooptical Instrumentation, (Prentice Hall, Upper Saddle River, NJ, 2004), Chap. 5, pp. 181–222.
[20] S. Donati, Electrooptical Instrumentation, (Prentice Hall, Upper Saddle River, NJ, 2004), Chap. 6, pp. 223–246.
[21] S. Donati, L. Falzoni, and S. Merlo, IEEE Trans. Instrum. Meas. **45**, 942–947 (1996).
[22] R. S. Vodhanel, M. Krain, and R. E. Wagner, in: Proceedings of the Conference on Optical Fiber Communication (OFC'94), San Jose 1994, paper WG-5, pp. 103–104.
[23] S. Donati and G. Martini, J. Opt. Soc. Am. **69**, 1690–1694 (1979).
[24] M. Norgia, S. Donati, and D. d'Alessandro, IEEE J. Quantum Electron. **37**, 800–806 (2001).
[25] see http://www-3.unipv.it/donati/SM_Interfer_UniPV.pdf.
[26] S. Merlo and S. Donati, IEEE J. Quantum Electron. **31**, 113–119 (1995).
[27] G. Plantier, C. Bes, and T. Bosch, IEEE J. Quantum Electron. **41**, 1157–1167 (2005).
[28] G. Giuliani, S. Bozzi-Pietra, and S. Donati, Meas. Sci. Technol. **14**, 24–32 (2003).
[29] see http://www-3.unipv.it/donati/SMVibro_UniPV.pdf.
[30] B. Boashash, Proc. IEEE **80**, 519–569, (1992).
[31] T. G. Giallorenzi, J. A. Bucaro, A. Dandridge, G. H. Siegel, J. H. Cole, S. C. Rashleigh, and R. G. Priest, IEEE J. Quantum Electron. **18**, 626–665 (1982).
[32] L. Scalise, Y. Yu, G. Giuliani, G. Plantier, and T. Bosch, IEEE Trans. Instrum. Meas. **53**, 223–229 (2004).
[33] G. Giuliani, M. Norgia, S. Donati, and T. Bosch, J. Opt. A, Pure Appl. Opt. **4**, S283–S294 (2002).
[34] M. Liess, G. Weijers, C. Heinks, A. van der Horst, A. Romers, P. Duijve, and G. Mimnagh, IoP Meas. Sci. Technol. **13**, 2001–06 (2002).
[35] F. Gouaux, N. Sarvagent, and T. Bosch, Appl. Opt. **37**, 6684–6689 (1998).
[36] M. Norgia, G. Giuliani, and S. Donati, IEEE Trans. Instrum. Measure. **56**, 1894–1900 (2007).
[37] H. Matsumoto, Appl. Opt. **19**, 1–2 (1980).
[38] G. Giuliani, S. Donati, M. Passerini, and T. Bosch, Opt. Eng. **40**, 95–99 (2001).
[39] G. Giuliani and M. Norgia, IEEE Photon. Technol. Lett. **12**, 1028–1030 (2000).
[40] Y. Yu, G. Giuliani, and S. Donati, IEEE Photon. Technol. Lett. **16**, 990–992 (2004).
[41] J. Xi, Y. Yu, J. Chicharo, and T. Bosch, IEEE J. Quantum Electron. **41**(8), 1058–1064 (2005).

[42] A. Villafranca, J. Lasobras, I. Garces, G. Giuliani, and S. Donati, and further 28 authors, in: Proceedings of Conference on Lasers and Electro-Optics (CLEO), Baltimore 2007, paper CThK-1.

[43] S. Odermatt and B. Witzigmann, IEEE J. Quantum Electron. **42**(8), 538–554 (2006).

[44] M. Fathi and S. Donati, Opt. Lett. **35**, 1844–46 (2010).

[45] T. Dresel, G. Hausler, and H. Venzke, Appl. Opt. **31**, 919–925 (1992).

[46] P. J. Caber, Appl. Opt. **32**, 3438–3441 (1993).

[47] S. Donati, V. Annovazzi Lodi, S. Merlo, and M. Norgia, in: Proceedings of the IEEE-LEOS Conference on Optical MEMS, Kawai, HI, 2000, pp. 89–90; IEEE Trans. Mechatron. **6**, 1–6 (2001).

[48] V. Annovazzi Lodi, M. Benedetti, and S. Merlo, IEEE J. Sel. Top. Quantum Electron. **10**, 536–544 (2004).

[49] S. Donati, M. Norgia, and G. Giuliani, Appl. Opt. **45**, 7264–7268 (2006).

[50] S. Donati, and V. Speziali, in: Proceedings of the Conference on Laser and Electrooptics Applicatione (CLEA), Washington 1977; Digest in IEEE J. Quantum Electron. **13**, 798-87D (1977); Laser Elektro-Opt. (West Germany) **12**, 34–35 (1980).

[51] J. Hast, R. Myllylä, H. Sorvoja, and J. Miettinen, IoP Quantum Electron. **32**, 975–982 (2002).

[52] L. Rovati, S. Cattini, and N. Palanisamy, IoP Meas. Sci. Technol. **23**, (2011), doi:025402.

[53] A. Pesatori, M. Norgia, and L. Rovati, IEEE Sensor J. **11** (2011), doi: JSEN2011.2131646.

[54] R. Kliese, Y. L. Lim, T. Bosch, and A. D. Rakić, Opt. Lett. **35**, 814–816 (2010).

[55] S. Donati and M. Sorel, IEEE Photon. Technol. Lett. **8**, 405–408 (1996).

[56] S. Donati and M. Sorel, in: Proceedings of the Optical Fiber Communication Conference, OFC'97, Dallas 1997, paper WJ8, p. 161.

[57] C.-H. Lu, J. Wang, and K.-L. Deng, Appl. Phys. Lett. **66**, 2022–2024, (1995).

[58] M. Wang and G. Lai, Opt. Commun. **238**, 237–244 (2004).

[59] H. Ukita, Y. Uenishi, and Y. Katagiri, Appl. Opt. **33**, 5557–5563 (1994).

[60] P. Dean, Y. L. Lim, A. Valavanis, R. Kleise, M. Nikolic, S. P. Khanna, M. Lachab, D. Indjin, Z. Ikonic, P. Harrison, A. D. Rakic, E. H. Lindfield, and G. Davies, Opt. Lett. **36**, 2587–2589 (2011).